Geochemical impacts of hydrothermal activity on surface deposits at the Southwest Indian Ridge

Anyang Pan [a, b, c], Qunhui Yang [a, *], Huaiyang Zhou [a, *], Fuwu Ji [a], Hu Wang [a], Richard D. Pancost [b]

[a] *State Key Laboratory of Marine Geology, School of Ocean and Earth Science, Tongji University, Siping Rd. 1239, Shanghai 200092,China*
[b] *Organic Geochemistry Unit, School of Chemistry, Cabot Institute, University of Bristol, Cantock's Close, Bristol BS8 1TS, UK*
[c] *SINOPEC Petroleum Exploration and Production Research Institute, Wuxi Institute of Petroleum Geology, 2060 Lihu Road, Wuxi, Jiangsu 213126, China*

* Corresponding author. Tel: +86 13918209499
E-mail address: yangqh@tongji.edu.cn (Qunhui Yang), zhouhy@tongji.edu.cn (Huaiyang Zhou)

Abstract

Submarine hydrothermal circulation has attracted much scientific interest since seafloor hydrothermal activity was first observed in the 1970s; an area of particular interest is the impact of exported inorganic and organic materials from hydrothermal vent systems into the open ocean. In 2007, the first active hydrothermal vent field, with vent fluid temperatures up to 379 °C, was discovered at the ultraslow spreading Southwest Indian Ridge (SWIR), where active vents are much less abundant than fast spreading ridges, and the effect of hydrothermal extrusion on surface sediments is not fully understood. To explore how geochemical proxy signatures respond to hydrothermal activity, we investigated the distributions of elements, minerals and lipids in surficial normal marine sediments, metalliferous sediments and low-temperature hydrothermal deposits collected from the SWIR. The results showed

different effects of hydrothermal activity on the surface deposits. The normal marine sediments were predominantly calcium carbonate characterized by >42% CaO and >90% calcite, with a significant autochthonous marine contribution to organic matter (OM) and a predominance of lower molecular weight alkanols and fatty acids; they were uninfluenced by hydrothermal activity but received some terrigenous input represented by abundant high molecular weight *n*-alkanes with an odd-over-even predominance. The near-field metalliferous sediments and hydrothermal deposits were very different. Some near-field metalliferous sediments were influenced by low-temperature hydrothermal activity, and their distributions of elements and minerals were similar to those of hydrothermal deposits, which were characterized by abundant Fe/Si and opal/nontronite. Other near-field metalliferous sediments were evidently influenced by mixing of high-temperature hydrothermal sulfides typically containing abundant Cu/Zn. With respect to the organic matter assemblages, near-field deposits contained little evidence for thermal maturation of organic matter and all were characterized by a strong microbial signature, including hopanoids, isoprenoidal and non-isoprenoidal dialkyl glycerol ether lipids, and low molecular weight *n*-alkanes with an even carbon number predominance. The far-field metalliferous sediments, despite the influence of non-buoyant plumes and slightly higher concentrations of hydrothermal-derived metals (e.g., Fe, Cu and Zn), had the same distribution of organic lipids and major mineral composition (>90% calcite) as did normal marine sediments. Thus, the influence of non-buoyant plume inputs appears to have been minimal possibly due to the dilution of in situ microorganisms

by normal marine organisms in sediment and seawater. Furthermore, these characteristics indicate inorganic indices based on abundant metal elements derived from the hydrothermal systems (such as Fe/Cu/Zn content, ∑REE/Fe, the ternary diagram of Fe, Cu×100 and Ca) are more sensitive, serving as better proxies than organic matter assemblages to differentiate the effects of diverse hydrothermal activity on surface deposits.

Keywords: element; mineral; lipid biomarker; in situ microorganisms; hydrothermal activity; Southwest Indian Ridge

1. Introduction

Hydrothermal circulation, a common process along mid–ocean ridges, plays an important role in global ocean cycles via significant inputs of reduced substrates, such as H_2S, H_2, CH_4, NH_3, Mn^{2+} and Fe^{2+}, which can fuel chemosynthetic microbial metabolism (e.g., de Angelis et al., 1993; Elderfield and Schultz, 1996; McCollom, 2000; Lam et al., 2004; Dick et al., 2009; Petersen et al., 2011; Dick et al., 2013), and even be a significant source of carbon to the deep ocean (e.g., McCollom, 2000; Lang et al., 2006; McCarthy et al., 2011). Previous hydrothermal studies have mainly focused on near-field hydrothermal products, such as sulfide structures (e.g., Kato et al., 2010; Peng et al., 2011b; Jaeschke et al., 2012; Gibson et al., 2013; Reeves et al., 2014), hydrothermally influenced sediments (e.g., Schouten et al., 2003; Shulga et al., 2010; Shulga and Peresypkin, 2012), and rising plumes (e.g., Bennett et al., 2011; Sands et al., 2012; Estapa et al., 2015), in relation to the characteristics of inorganic

(elements and minerals) and organic (lipids) geochemistry, biogeography and biodiversity. However, a growing number of studies have focused on the microbial ecology and biogeochemical cycles involving the transport of metals and organic carbon in non-buoyant plumes (e.g., Bennett et al., 2008; Bennett et al., 2011; Lesniewski et al., 2012; Sylvan et al., 2012; Li et al., 2015; Sander and Koschinsky, 2016). Of particular interest has been hydrothermally derived dissolved Fe, which can be dispersed over thousands of kilometers away from its source into the open ocean and contribute to the global oceanic Fe budget (e.g., Toner et al., 2012; Fitzsimmons et al., 2014, 2017; Resing et al., 2015; Kleint et al., 2016). However, the geochemical characteristics of the sediments influenced by such non-buoyant plumes remain largely unstudied.

Low-temperature hydrothermal systems with formation temperatures of <100 °C had previously been largely ignored but have recently become research hotspots. Relatively recent investigations of such settings have focused on biogeochemical cycling mechanisms of Fe, Mn, and S (e.g., Butterfield et al., 2004; Perner et al., 2007; Edwards et al., 2011; Sun et al., 2011, 2013, 2015) and the microbial ecology and biogeochemistry of low-temperature hydrothermal environments (e.g., Edwards et al., 2011; Peng et al., 2011a; Li et al., 2012; Li et al., 2013). These have confirmed that low-temperature settings have geochemical characteristics and microbial communities distinct from those of high-temperature hydrothermal systems (e.g., Blumenberg et al., 2012; Jaeschke et al., 2012; Gibson et al., 2013; Reeves et al., 2014).

Increasing attention is being paid to hydrothermal fields at the ultraslow

spreading Southwest Indian Ridge (SWIR) because more hydrothermal vents (including high-temperature and low-temperature hydrothermal fields) than expected were discovered since 2007 (e.g., Fujimoto et al., 1999; Münch et al., 2001 ; Bach et al., 2002; German, 2003; Tao et al., 2007, 2012), and there have been some reports on the petrology and element geochemistry (e.g., Tao et al., 2011, 2012; Cao et al., 2012; Gao et al., 2016; Li et al., 2016b) and molecular biology (e.g., Peng et al., 2011a; Li et al., 2013; Cao et al., 2014; Li et al., 2016a). However, research on lipid biomarkers in the SWIR hydrothermal systems remains rare (Huang et al., 2014; Lei et al., 2015). There are also relatively few studies on the effects of hydrothermal activity on the surrounding environment, especially the metalliferous sediments (Pan et al., 2016) formed via a combination of sulfide mass wasting and debris flow, low-temperature fluid flow and mineralization, or plume formation, dispersal and fallout (Dias et al., 2008).

The surface deposits (0-10cm) studied in this paper, including normal pelagic sediment, far-field and near-field metalliferous sediments, and low-temperature hydrothermal deposits, were collected from the first discovered active hydrothermal vent field, the Dragon Vent Field (49°39′ E, 37°47′ S), a nearby inactive field (50°28′ E, 37°39.50′ S) and surrounding areas (Fig. 1 and Supporting Information Table S1) during the DY115-20 and DY115-21 expeditions of the R/V Da Yang Yihao in 2009 and 2010, by using a television-video guided grab. These three distinct surface deposits provide an opportunity to explore the potential effects of hydrothermal activity on the surrounding sediments. Our previous study examining the distribution

of glycerol dialkyl (and monoalkyl) glycerol tetraether (GDGT and GMGT) archaeal membrane lipids (Pan et al., 2016) clearly showed that GDGT distributions in normal marine sediments, near-field metalliferous sediments and low-temperature hydrothermal deposits vary significantly, whereas the far-field metalliferous sediments have the same GDGT distribution as that of the background sediments. Here, we present new comprehensive data of mineralogy, element geochemistry and other lipid biomarkers (alkanes, hopanoids, alkanols and fatty acids) to explore further how hydrothermal activity affects the (inorganic and organic) geochemistry of the surrounding sediments and to broaden the understanding of hydrothermal circulation and the roles of microorganisms in biogeochemical cycling at the SWIR.

2. Methods

2.1. Elemental and mineral analysis

Major and trace elements were analyzed in the State Key Laboratory of Marine Geology, Tongji University. The freeze-dried deposit samples were ground into powder, then combusted in a muffle furnace at 600 °C for 4 h to oxidise the OM. 30 to 50 milligrams of combustion products were then digested with concentrated HNO_3 and HF, and this was followed by heating at 150 °C for 24 h. The digests were then evaporated to dryness (×2). Samples were diluted with 2% HNO_3 before analysis. The concentration of major and trace elements was determined via Inductively Coupled Plasma-Optical Emission Spectrometry (ICP-OES, Thermo fisher IRIS Advantage) and Inductively Coupled Plasma-Mass Spectrometry (ICP-MS, Thermo fisher VG-X7

mass spectrometer), respectively. The precision and accuracy were monitored by replicate analyses of geostandards GSR-5, GSR-6, and GSD-9, and the relative deviations between the measured and certified values were less than 5% for most elements.

For mineral analysis, the X-ray diffraction (XRD) pattern analysis of powdered samples was performed at the Guangzhou Institute of Geochemistry, Chinese Academy of Sciences (CAS), by using an X-ray diffractometer (Bruker-D8 Advance, German) with a Ni-filtered Cu Kα radiation source at 40 kV and 30 mA. Diffraction angles (referred to as "2θ") ranged from 3–85°. The scan speed was 4°/min. Qualitative and semi-quantitative characterization of mineralogy and other details have been presented in He et al. (2010).

2.2. Lipid biomarker analysis

Two methods were used successively for different samples and have been described in detail in Pan et al. (2016). Because GDGTs analyzed by high-performance liquid chromatography/atmospheric pressure chemical ionization-mass spectrometry (HPLC/APCI-MS) exhibit distinct differences among sediment types (Pan et al., 2016), other lipid biomarkers were examined here to further explore differences.

Briefly, the total lipid extracts obtained were separated into three fractions: simple core lipids (CLs), glycolipids (GLs) and phospholipids (PLs). Metalliferous sediments (M-T2 and M-T3) and hydrothermal deposits were processed with method

1, which used a Bligh-Dyer extraction (Bligh and Dyer, 1959) and fractionation protocol based on that in Dickson et al. (2009), in which chloroform:acetic acid (100:1, v:v), acetone and methanol were used to recover each respective fraction through a silica column. The CL fraction was eluted through another silica column with chloroform saturated with ammonium hydroxide and chloroform:acetic acid (100:1, v:v) to separate neutral components and free fatty acids (FFAs), respectively. Method 2 used ultrasonication (Schouten et al., 2002) and a fractionation protocol detailed in Pitcher et al. (2009), and the elution solvents hexane:ethyl acetate (3:1, v:v), ethyl acetate and methanol were used for passing each respective fraction through a silica column; this method was used for the background sediments and M-T1. For both methods, the GL and PL fractions were hydrolyzed and heated at 100 °C for 3 h with 5% HCl in methanol.

Although these two protocols yield reproducible GDGT distributions, allowing a comparison of those compounds for the entire sample set (Pan et al., 2016), the recovery and separation of bacterial and eukaryotic lipids between them might not be consistent. Therefore, we focus on 1) a qualitative comparison of neutral lipid distributions across all samples (i.e. those eluted in the CL fraction of Method 2 or the neutral lipid fraction of Method 1); and 2) a semi quantitative comparison of fatty acid distributions in MT1and background sediments (all processed using Method 2).

Gas chromatography-mass spectrometry (GC-MS) analysis was performed at the Organic Geochemistry Unit (OGU), School of Chemistry, University of Bristol, with instrument conditions as follows: ThermoQuest Trace GC interfaced to Finnigan

Trace MS quadrupole spectrometer, electron impact ionization (70 eV), full scan mode (*m/z* 50-650), HP-1 capillary column (50 m × 0.32 mm i.d.; 0.17 μm film thickness), He carrier gas. Samples were derivatized with N, O-Bis(trimethylsilyl) trifluoroacetamide (BSTFA, Sigma Aldrich) at 70 °C for 1 h before GC-MS analysis and injected at 70 °C with a temperature program of 20 °C/min to 130 °C and 4 °C/min to 300 °C (held 25 min). The internal standards for apolar and polar components in the neutral fraction were 5α-androstane and hexadecane-2-ol, respectively.

3. Results

3.1. Bulk Geochemistry and Mineralogy

There were significant differences in the elemental and mineral compositions of the different surface deposits (shown in Table 1 and Supporting Information Table S1). Although we determined abundances of numerous elements, here we initially focus on Fe, Cu and Ca to distinguish the surface deposits into major groups (Fig. 2). We focus on Fe because solubilized hydrothermal Fe can be transported kilometers away from vent sites (Toner et al., 2012; Fitzsimmons et al., 2014; Resing et al., 2015; Kleint et al., 2016). Hydrothermally sourced elemental Cu is often enriched in high-temperature hydrothermal products and falls out of the plume more rapidly than Fe (Cave et al., 2002). We consider Cu and Fe relative to Ca, because background sediments of the SWIR are dominated by calcium carbonate deposition. All studied samples were classified into three categories (Fig. 2):

(1) Pelagic sediments far from hydrothermal vents (termed background sediments): these samples were characterized by CaO as the major element (44% average), and low abundances of of Al, Fe, K, Mg, Mn, Na, P and Ti (Table 1). Although biophile elements, such as Ba and Sr, had markedly high abundances (290 ppm and 1400 ppm on average, respectively), other trace elements (e.g., V, Cr, Co, Ni, Cu, Zn, Mo and Pb) occurred in only very low abundances. Calcite is the major mineral (>90%) in these samples.

(2) Metalliferous sediments: these samples were divided into three subtypes. Metalliferous type 1 sediments (M-T1, far-field product), including SW2, SW3 and SW4 located near the Dragon Vent Field and SW10 located close to the inactive field, contained slightly higher abundances of Al, Ti, Fe, V, Cr, Ni, Cu and Zn relative to background sediments (Fig. 3a), although they were still dominated by Ca as the major element and calcite as the major mineral. In contrast, other metalliferous sediments (near-field product) had higher Fe, Mn, Na, P, V, Co, Ni, Cu, Zn and Mo contents and a lower Ca content. These samples were divided into two further types: metalliferous type 2 sediments (M-T2, samples SW32, SW38 and SW39) and metalliferous type 3 sediments (M-T3, samples SW35 and SW40). These were distinguished on the basis of mineralogy, with M-T2 sediments containing nontronite and two-line-ferrihydrite and lower Al, Ti and Cr contents (Fig. 3b), and M-T3 sediments containing abundant Fe, Mn, Cu and Zn (Fig. 3c; with Cu especially high up to 11000 ppm). Of the M-T3 sediments, SW35 was composed of calcite and aragonite, and SW40 was composed of goethite and illite/smectite, showing distinct

mineral compositions from those of M-T2.

(3) Hydrothermal deposits enriched in Fe and/or Si: compared with the concentrations in background sediments, the Al, Ti, Cr, Ni and Ca contents were much lower, and the P, V, Mn, Fe, Cu, Zn and Mo contents were higher (Fig. 3d, Table 1). Although the Si content was not directly measured in these hydrothermal deposits, Si is known to be another important major element in these hydrothermal deposits because of the mineral composition (mainly opal and nontronite) and concentrations of Si (22–89%) in deposits from the same sites (SW33, SW35, SW36) are high (Peng et al. (2011a) and Li et al. (2013)).

The distribution of rare earth elements (REE) varied among these samples. The total REE content (ΣREE) was highest in background sediments, with a range of 13–41 ppm (24 ppm average), and most metalliferous sediments (M-T1, M-T2 and M-T3), with a similar range of 18 to 31 ppm. The total REE content was lowest in hydrothermal deposits, at 0.66–8.2 ppm (3.6 ppm average) (Table 1). All sediments exhibited a characteristic enrichment of light REE (LREE) and a relative depletion in heavy REE (HREE), but had different LREE/HREE values, with ranges of 3.6–5.4, 2.8–3.5, 1.7–3.1, 2.4–3.3 and 1.7–7.6 in background sediments, M-T1, M-T2, M-T3 and hydrothermal deposits, respectively (Supporting Information Table S1).

North American shale composite-normalized REE distribution patterns of surface deposits showed the same characteristics of a left-leaning LREE and a relatively flat HREE but had different Ce and Eu anomalies (Fig. 4, Table 1 and Supporting Information Table S1). Weak-moderate negative Ce anomalies were present in most

samples, with δCe exhibiting ranges of 0.48–0.83, 0.57–0.82, 0.39–0.73, 0.54–0.72 and 0.34–1.0 for background sediments, M-T1, M-T2, M-T3 and hydrothermal deposits, respectively; there were generally no anomalies in Eu for background sediments and M-T1 (δEu=1.1–1.4 and 1.2–1.4, respectively), but positive Eu anomalies occurred in M-T2 and M-T3 (δEu=1.3–7.9 and 1.5–1.8, respectively), and especially in hydrothermal deposits (δEu= 3.1–56).

3.2. Distributions of biomarkers in background sediments and M-T1

In contrast to elemental compositions, there were no significant distinctions in organic lipid compositions between background sediments and M-T1 (Table 2), a result similar to the GDGT compositions discussed in Pan et al. (2016). Among the 'neutral lipids' of both background sediments and M-T1, high molecular weight (HMW) *n*-alkanes (n-C_{22}–n-C_{34}) were dominant (range 68%–86%) and characterized by an odd-carbon predominance with the carbon preference index (CPI, defined by Bray and Evans, 1961) values in the range of 1.0 to 4.5, peaking at n-C_{31}. The average chain length (ACL) of total *n*-alkanes ranged from 25 to 28. The average values of HMW proportions, CPI and ACL for background sediments were 79%, 2.8 and 27, respectively, which were very similar to those of M-T1 (82%, 3.0 and 27, respectively). Long chain C_{37}–C_{39} unsaturated methyl and ethyl ketones were found in both M-T1 and background sediments, such as 37:3, 37:2, 38:3 and 38:2 methyl alkenones, 38:3 and 38:2 ethyl alkenone, which were derived from marine phytoplankton, especially Coccolithophores, and used to reconstruct past sea-surface

temperature (Brassell et al., 1986).

The distribution of *n*-alkanols in M-T1 and background sediments was typical for pelagic sediments as well, dominated by low molecular weight (LMW) compounds (*n*-C_{12}–*n*-C_{21}) with LMW to HMW ratios (*n*-C_{21}^{-}/*n*-C_{22}^{+}) in the range from 3.3 to 20, peaking at *n*-C_{18}. The most abundant sterol detected was cholesterol, generally considered to be mainly derived from marine zooplankton and only minor from phytoplankton (Volkman, 1986). A few of other sterols (e.g., sitosterol, found in higher plants, Goad and Goodwin, 1972) and very low abundances of stanols can be identified.

The fatty acid (FA) distributions – in all three fractions – did not differ between M-T1 and background sediments (See Fig. 5). This is true even for the phospholipid fatty acids (PLFAs) which might have been expected, as biomarkers for 'living biomass', to have been impacted by the metal inputs. For both free fatty acids (FFAs) and PLFAs, M-T1 and background sediments were dominated by saturated fatty acids (SFAs, >90%), with a slightly higher proportion of monounsaturated fatty acids (MUFAs) than branched fatty acids (BrFAs). The glycolipid fatty acids (GLFAs), were dominated by MUFAs (>60%) in both sediment types, followed by SFAs, and lower proportions of BrFAs and polyunsaturated fatty acids (PUFAs).

The SFAs, like the *n*-alkanols, were dominated by lower molecular weight fatty acids in each fraction (C_9–C_{21}, a maximum at *n*-$C_{16:0}$, Fig. 5; LMW to HMW ratios >>1, Table 2). The BrFAs were mainly *br*C_{15}, *br*C_{16} and *br*C_{17}, including the *iso* and *anteiso* components. It is noteworthy that the near-field metalliferous sediments

and hydrothermal deposits had greater abundance of BrFAs derived from bacteria than M-T1 and background sediments as mentioned in Pan et al. 2016. $C_{18:1\omega9}$ was the dominant MUFA in both the FFA and PLFA fractions, whereas $C_{18:1\omega9}$ and $C_{22:1}$ were the major MUFAs in GLFAs (Fig. 5), with minor contributions from $C_{16:1\omega7}$, $C_{20:1}$ and $C_{24:1}$ MUFAs.

3.3. Specific biomarker compositions in near-field metalliferous sediments and hydrothermal deposits

In our previous study (Pan et al., 2016), we showed that the GDGT compositions of near-field metalliferous sediments (M-T2 and M-T3) and hydrothermal deposits are markedly different from those in background sediments and M-T1, and are characterized by high relative abundances of isoprenoid GDGTs bearing multiple rings, the presence of GMGTs, and relatively low abundances of crenarchaeol. Here, we probe those differences further by examining the distributions of alkanes, hopanoids and alcohols found in this study (Table 3). We note that although different lipid analysis methods have been used, there is no evidence that they have affected the distributions of these specific compound classes.

Among the *n*-alkanes, M-T2 and M-T3 sediments were characterized by LMW homologues with an even-over-odd carbon number predominance (*n*-C_{16}, *n*-C_{18} and *n*-C_{20}), showing lower values of HMW percent (30%–39%, 35% average), CPI (0.41–1.0, 0.71 average) and ACL (18–20, 19 average). We observed the same for hydrothermal deposits SW31, SW33, SW36 and SW37, with ranges of 33%–50%

(41% average), 0.24–0.80 (0.53 average) and 20–21 (21 average) for HMW percent, CPI and ACL, respectively, although *n*-alkanes were nearly undetected in hydrothermal deposits SW41, SW45 and SW46 (Table 3). This differs markedly with the distributions in M-T1 and background sediments, dominated by HMW *n*-alkanes of likely higher plant origin (Eglinton and Hamilton, 1967; see above).

We did not analyse intact bacteriohopanepolyols and focus here on the hopanoids present in the core lipid fraction; these include the geohopanes potentially formed by thermal alteration of bacterial biomass (Simoneit et al., 2004) and biological hopanoids, such as diploptene (Ⅰ, all chemical structures are shown in the Appendix; de Rosa et al., 1971; Rohmer et al., 1984), diplopterol (Ⅱ; Rohmer et al., 1984; Pancost et al., 2000) and 17β,21β(H)-bishomohopan-32-ol (which likely derives from degradation of bacteriohopanetetrol; Farrimond et al., 2000). In the M-T1 and normal marine sediments, hopanoids were present in only trace abundances. However, in the M-T2 and M-T3 sediments as well as the hydrothermal deposits (except for SW36 and SW37, Table 3), hopanoids were abundant. Immature hopanoids dominated, including trisnorhopan-21-one (Ⅲ), 17β,21β(H)-hopan-30-ol (Ⅳ) and 17β,21β(H)-bishomohopan-32-ol, all of which are likely oxidation/cleavage products from bacteriohopanepolyol precursors (Simoneit et al., 2004). Also present, although in subordinate abundances, were diploptene and diplopterol, derived from various bacteria (de Rosa et al., 1971; Rohmer et al., 1984; Pancost et al., 2000). Similarly, the geohopanes predominantly occurred as the immature isomers – 17β,21β(H)-hopanes (Ⅴ).

However, more thermally mature hopanes, including both moretanes [17β,21α(H)-hopanes, Ⅵ] and lesser amounts of the thermally favoured 17α,21β(H)-hopanes (Ⅶ) were also present (except for SW39). During hydrothermal maturation, hopanoids can isomerize, converting the 17β,21β(H) configuration of >C_{31} hopane homologues into the more thermally stable 17α,21β(H) configuration. Similarly, epimerisation at the C-22 position results in a mixture of S and R epimers (22S)/(22S+22R), ultimately reaching the equilibrium ratio of about 0.6 (Seifert and Moldowan, 1978). The homohopane epimer ratios in the studied samples ranged between 0.41 and 0.52, not fully mature as observed in other hydrothermal settings (e.g., Rushdi and Simoneit, 2002; Simoneit et al., 2004; Lei et al., 2015) but indicating some hydrothermal alteration.

Perhaps most striking, non-isoprenoidal dialkyl glycerol diethers (DGDs, Ⅷ), macrocyclic glycerol diethers (McGDs, Ⅸ), and archaeol (Ⅹ, discussed in Pan et al., 2016) were detected in M-T2 and M-T3 sediments and hydrothermal deposits (Table 3) but not in M-T1 and normal marine sediments. The alkyl chains of DGDs ranged in carbon number from C_{13} to C_{19}, including a predominance of C_{15}/C_{15} or C_{17}/C_{17}, and the alkyl chain of the McGDs ranged from C_{31} to C_{35}. This provides strong evidence that hydrothermal processes have impacted the microbial assemblages in near-field sediments, with likely source organisms discussed below.

4. Discussion

Hot fluids, emitted from hydrothermal vents, can rise hundreds of meters into the

overlying water column through buoyancy; when the water reaches a density identical to that of the background seawater, the plume becomes non-buoyant and spreads laterally. This not only transports inorganic chemical components to the background seawater around hydrothermal vents (e.g., Fe, Mn, Cu, Zn, Cave et al., 2002) but also microorganisms and biogenic and abiogenic OM (see review by Konn et al., 2011). Here we explore how the plume from the hydrothermal fields of the SWIR impacted both metal and organic matter in near-field (<0.1 km) and more distal sediments (~0.8 km).

4.1. Distinct inorganic compositions of surface deposits clearly reflect different effects of hydrothermal activity

The ternary diagram of Fe, Cu×100 and Ca distinguishes all of the surface deposits into three categories: background sediment, metalliferous sediments (further divided into M-T1, M-T2 and M-T3 subtypes) and low-temperature hydrothermal deposits (Fig. 2). Each category and subtype has specific elemental and mineral compositions.

The hydrothermal and detrital contributions to sediments can be estimated from the ratios of Fe/Ti vs Al/(Al+Fe+Mn) (Boström et al., 1973; Dias and Barriga, 2006; Slack et al., 2009). In Fig. 6, all hydrothermal deposits should lie on the theoretical curve, and the increase in Al/(Al+Fe+Mn) and decrease in Fe/Ti along that curve indicates the dilution of metalliferous sediments with pelagic sediments. The background sediments had Al/(Al+Fe+Mn) ratios greater than 0.4 (the minimum

value in pelagic deep-sea sediments, Boström et al., 1973); moreover, the Fe, Mn, Cu and Zn contents were low, and the REE distribution was similar to that of seawater, with negative Ce anomalies (Fig. 4a), all indicating that the background sediments were scarcely affected by hydrothermal activity. The mineral calcite and the element Ca were dominant in background sediments, thus suggesting that dissolution of deep-sea carbonate was not occurring and consistent with sediments being above the carbonate compensation depth (>5000 m, Van Andel, 1975). These biogenic calcites were comprised of calcareous nannofossils and foraminifera (Chen et al., 2013), and a similar composition has been found in sediments from the Central Indian Ocean (Littke et al., 1991).

The Fe/Ti ratios in hydrothermal deposits (or Fe-Si oxide precipitates) from the SWIR were much larger than those in other sediments, whereas Al/(Al+Fe+Mn) ratios were lower, lying on the theoretical curve of hydrothermal sources (Fig. 6). The hydrothermal deposits also showed significant positive Eu anomalies and moderately weak negative Ce anomalies (Fig. 4e), with low REE content, thus indicating that these samples inherited the characteristics of hydrothermal fluid and were less influenced by seawater and the mixing of background sediments. Previous studies have shown that Fe-Si oxide precipitates are easily formed at relatively low temperatures (<100 °C) in chimney structures and under diffuse flow conditions and are composed of amorphous silica and poorly crystalline phases, especially ferrihydrite, as well as crystalline iron-rich silicates, such as nontronite (Sun et al., 2011, 2012, 2013). These minerals were also abundant in the hydrothermal deposits

from the SWIR. Li et al. (2013), using the oxygen isotopic compositions of amorphous silica in some of these hydrothermal deposits (SW33 and SW36), concluded that the formation temperature ranged from 38 to 82 °C, confirming that these hydrothermal deposits were largely formed through low-temperature hydrothermal activity. The enrichment of Fe, Si and P might be related to the presence of Fe-oxidizing bacteria (FeOB), as suggested by SEM analysis of Fe-Si oxyhydroxide deposits elsewhere in the SWIR (Sun et al., 2015).

The SWIR metalliferous sediments, based on their elemental and mineral composition, span the range between the background and hydrothermal end-members. The Fe/Ti and Al/(Al+Fe+Mn) ratios, δCe, δEu, Ca content, ∑REE and the REE distribution pattern (Fig. 4b) in M-T1 sediments were very similar to those in background sediments. However, the abundance of elements typically enriched in hydrothermal plume particles (e.g., Fe, Cu, Zn, P, V; Cave et al., 2002), was relatively high in M-T1 sediments, indicating that they were influenced by fallout from hydrothermal plumes originating in the nearby hydrothermal fields. ∑REE/Fe can be used as a relative measure of paleodistance between the location of the hydrothermal vent and the site of the plume fallout to sediments and to show the relative strength of the effects of hydrothermal activity (Ruhlin and Owen, 1986). The ∑REE/Fe ratios in M-T1 were between those of background sediments and other metalliferous sediments (Table 1 and Supporting Information Table S1), consistent with M-T1 sediments being located far from the hydrothermal vent and experiencing weak effects of hydrothermal activity (non-buoyant plume) and a strong influence from seawater

(German et al., 1990; German et al., 1999).

Compared with background sediments and M-T1, the near-field metalliferous sediments (M-T2 and M-T3) were strongly affected by hydrothermal activity. They contained more Fe, Mn, Cu, Zn and Mo, and less Ca and Sr, similar to the hydrothermal deposits (Noll et al., 1996; Cave et al., 2002), and were generally located near the hydrothermal end-member in Fig. 6; however, M-T2 and M-T3 sediments had less positive Eu anomalies and higher ∑REE content than SWIR hydrothermal deposits (Fig. 4c, 4d and Table 1). The mineral compositions of the M-T2 sediments (nontronite and two-line-ferrihydrite) were analogous to those of the low-temperature hydrothermal deposits, clearly indicating the major effects of low-temperature hydrothermal activity, such as low-temperature fluid flow and mineralization (e.g., Metz et al., 1988; German et al., 1993; Mills and Elderfield, 1995). M-T3 sediments (SW40 and SW35) had different mineral compositions and the highest Fe, Mn, Cu and Zn contents of all studied samples; this was especially true for Cu, which can rapidly fall out of plumes as sulfides or high-temperature hydrothermal products (Cave et al., 2002). Therefore, M-T3 sediments appear to have been formed by sulfide mass wasting and debris flow (Dias et al., 2008). Though the Al/(Al+Fe+Mn) ratio in SW35 was larger than that in other metalliferous sediments, it was still below 0.4 (Boström et al., 1973; Dias and Barriga, 2006). Moreover, the high calcite contents could indicate a higher proportion of background sediment mixing at SW35 compared with other metalliferous sediments.

4.2. The effect of a non-buoyant plume on the organic composition of surface deposits

Based on inorganic geochemical results, M-T1 appears to have been affected by a non-buoyant plume. Previous studies have indicated that particle organic carbon (POC) concentrations are elevated within hydrothermal plumes compared with background seawater (e.g., Bennett et al., 2011; German et al., 2015); thus, it is expected that M-T1 should have exhibited some differences in OM composition from background sediments.

However, all of the new biomarker analyses reported here, across multiple compound classes and diverse organic matter fractions, failed to reveal significant differences between M-T1 and background sediments. These results are the same as our previous research of GDGTs distribution (Pan et al., 2016). Li et al. (2016a) also reported no significant differences in the microbial compositions between far-field non-buoyant plumes (nearly co-located seawater samples of SW2, SW3 and SW4 of M-T1) and ambient seawater at the SWIR. Moreover, similar results have also been found in the Guaymas Basin and Eastern Lau Spreading Centers (ELSC) hydrothermal plumes (Lesniewski et al., 2012; Sheik et al., 2015). Therefore, we suggest that in these cases, the hydrothermal plume exerts a modest or no impact on far field organic matter assemblages, due to the lack of distinctive microbial communities thriving in the plume itself.

The same lipid compositions between M-T1 and background sediments suggest the same major sources of organic matter. The *n*-alkanes are dominated by HMW with larger ACL values (>25) and have an odd carbon dominance with average CPI>2 –

similar to *n*-alkane distributions in sediments from the Central Indian Ocean (Littke et al., 1991) and the South East Indian Ridge (Kim et al., 2009). This suggests the input of terrigenous higher plant (leaf wax) material to our study sites. However, terrigenous OM inputs were generally low due to the remoteness from any landmass (Pan et al., 2016). The low abundances of branched GDGTs in these sites (Pan et al., 2016), which are typically attributed to fluvially transported soil OM (Schouten et al., 2013 and references therein), are more likely caused by aeolian transport due to the sites far away from the land (Fietz et al., 2013). Compared with the low abundances of branched GDGTs, the contents of HMW *n*-alkanes derived from long distance aeolian transport (e.g., Poynter et al., 1989; Simoneit et al., 1991) are relatively higher, which has been documented by Fietz et al. (2013). The presence of low molecular weight alkanols and FAs, and especially BrFAs and unsaturated FAs, provides evidence for additional sources of organic matter, including both algal contributions and sedimentary bacteria (Dai and Sun, 2007 and references therein). The compositions of long chain unsaturated alkenones and dominant cholesterol reflect the contribution of phyto- and zooplankton communities to sedimentary OM.

4.3. Impact of hydrothermal activity on organic matter in near-field sediments

In contrast to far-field sediments, organic matter in the near-field deposits (M-T2 and M-T3 sediments) were strongly affected by indigenous chemosynthetic contributions to OM, with features similar to those of the low-temperature hydrothermal deposits at the SWIR. This is evident from previously reported

tetraether lipid distributions (Pan et al., 2016), which were characterized by GDGTs bearing elevated numbers of cyclopentyl moieties and the unusual presence of GMGTs. Our new data reinforces that interpretation.

The hydrocarbon fractions of these samples were dominated by LMW, even carbon number *n*-alkanes (C_{16}, C_{18} and C_{20}), similar to a distribution observed in oxy-altered sulfides from the SWIR (Lei et al., 2015) and likely indicative of a strong contribution of bacteria to sedimentary OM (Nishimura and Baker, 1986; Mille et al., 2007). Second, the sediments contained abundant bacterially derived hopanoids (Simoneit et al., 2004), although their greater abundance here compared to background sediments likely reflects both greater bacterial production but also hydrothermal alteration of bacteriohopanepolyols (see below).

Most diagnostic for the microbial assemblages in the M-T2, M-T3 and low-temperature hydrothermal deposits are the DGDs, major membrane lipids of some thermophilic bacteria, such as *Thermodesulfobacterium commune* (Langworthy et al., 1983), *Aquifex pyrophilus* (Huber et al., 1992), other *Aquificales* (Jahnke et al., 2001), and *Ammonifex degensii* (Huber et al., 1996). DGDs have also been detected in some non-thermophilic sulfate-reducing bacteria (SRB), such as *Desulfosarcina variabilis* and *Desulforhabdus amnigenus* (Rütters et al., 2001), as well as some species involved in anaerobic oxidation of methane (AOM) (Pancost et al., 2001; Elvert et al., 2005; Niemann and Elvert, 2008). Because *Aquificales* was absent in samples from the same sites at the SWIR (Peng et al., 2011a; Li et al., 2013) and the alkyl units of DGDs (C_{13}-C_{19}) in our samples were lower than those of *Aquificales* (C_{17}-C_{21})

(Jahnke et al., 2001), we discount that as a potential source. However, DGDs could have been derived from relatively abundant sulfate reducing δ-proteobacteria in these samples (Peng et al., 2011a; Li et al., 2013), similar to the inferred source in carbonate chimney structures at the Lost City hydrothermal field of the Mid-Atlantic Ridge (Bradley et al., 2009). Additionally, we cannot preclude contributions from other organisms, including thermophiles (e.g., Pancost et al, 2005, 2006; Kaur et al., 2008, 2011, 2015) or *Planctomycetes* (the latter having been detected here, Li et al., 2013, and a potential producer of DGDs, Sinninghe Damsté et al., 2002).

Also present were the even less common non-isoprenoidal McGDs. These were detected in some metalliferous sediments and low-temperature hydrothermal deposits from the SWIR, where there distributions were similar to those from New Zealand geothermal sinters (Pancost et al., 2006) and hydrothermal sulfides from the Mid-Atlantic Ridge (Blumenberg et al., 2007). The biological source of non-isoprenoid McGDs is still unclear, but an extremophilic bacteria source has been suggested (thermophilic and/or halophilic, Baudrand et al., 2010).

In addition to being distinguished from background sediments by the presence of a stronger and unique bacterial and archaeal biomarker signature, near-field metalliferous sediments could contain biomarkers impacted by hydrothermal alteration. One potential indicator is the *n*-alkane CPI (<1.0), as noted in previous studies, including the Middle Valley at the Juan de Fuca Ridge (Rushdi and Simoneit, 2002), the Rainbow vent field at the Mid-Atlantic Ridge (Simoneit et al., 2004), and the Dragon Vent Field at the SWIR (Lei et al., 2015). Hydrothermal alteration

signatures do seem to have been recorded by the hopanes, which occurred in both the biological precursor (17β,21β(H)) but also thermally altered 17β,21α(H) and 17α,21β(H) forms. However, the fact that the latter are subordinate indicates that the OM has been less 'matured' than that in other high-temperature hydrothermal sulfides and hydrothermal petroleum (e.g., Rushdi and Simoneit, 2002; Simoneit et al., 2004; Lei et al., 2015).

Collectively, all biomarker data indicate that the near-field metalliferous sediments (M-T2 and M-T3), formation via deposition from buoyant hydrothermal plumes (with sources of fluid inputs including focused vent flow, diffuse vent flow and entrained seawater, German et al., 2015) and weathering of hydrothermal deposits, has dictated the nature of organic matter preserved there; crucially, these biomarker distributions are distinct from those of far-field metalliferous sediments. This signature could arise from either direct deposition of organic matter via the plume or stimulation of unique microbial assemblages in these sediments. If the former, we would expect similar biomarker signatures in the far-field sediments and so we suggest that unique microbial assemblages are being produced in near-field sediments due to their unique chemistry and inoculation with hydrothermal organisms. This interpretation is consistent with a recent study of hydrothermal plumes at the ELSC that reveal that species richness and phylogenetic diversity are highest near the vent orifice because of the mixing of microbial communities from the surrounding habitats, whereas plume communities are more similar to pelagic communities because of background seawater dilution (Sheik et al., 2015). By extension, these specific

biomarkers did not serve as well as inorganic metal indices to distinguish M-T3 sediments influenced by high-temperature hydrothermal activity from M-T2 and low-temperature hydrothermal deposits; or to distinguish far-field plume M-T1 sediments from background sediments.

5. Conclusion

Through further analysis of surface deposits discussed in Pan et al. (2016), we have elucidated the geochemical characteristics of various surface deposits in and around a newly discovered hydrothermal vent system in the SWIR and explored the response of geochemical proxies in those surface deposits to hydrothermal activity. Our results indicate that hydrothermal activity has a remarkable effect on the elemental and mineral compositions of surface deposits, with Fe/Si and opal/nontronite enriched in the near-field deposits influenced by low-temperature hydrothermal activity; abundant Fe/Mn/Cu/Zn in the other near-field metalliferous sediments influenced by high-temperature; and slightly higher metal content (e.g., Fe, Cu and Zn) in far-field deposits than background sediments. However, our organic geochemical analyses reveal that the non-buoyant plume had limited impact on the microbiology or OM composition of far-field deposits. In contrast, in situ microorganisms (although perhaps originally derived from the hydrothermal environment via the plume) significantly contribute to the OM of near-field deposits. Compared with the indices based on abundant metal elements derived from the hydrothermal systems (such as Fe/Cu/Zn content, $\sum$REE/Fe, the ternary diagram of

Fe, Cu×100 and Ca), lipid biomarkers only partially differentiate the effects of diverse hydrothermal activity on surface deposits possibly due to the upper temperature limit of life impacting on organic matter assemblages and/or the dilution of in situ microorganisms by normal marine organisms in sediment and seawater.

Acknowledgments

We thank the captain and crew of the R/V Da Yang Yihao for assistance with sampling in the DY115-20 and 21 cruises. We also thank the staff in the Organic Geochemistry Unit and the Bristol Node of the NERC Life Sciences Mass Spectrometry Facility for analytical support. RDP acknowledges the RS Wolfson Research Merit Award. The work was funded by the Chinese National Key Basic Research Program (973 program, No. 2012CB417300), the National Natural Science Foundation of China (No. 41376048), and the Project of China Ocean Mineral Resources R & D Association (No. DY135-S1-1-10).

References

Bach, W., Banerjee, N.R., Dick, H.J.B., Baker, E.T., 2002. Discovery of ancient and active hydrothermal systems along the ultra-slow spreading Southwest Indian Ridge 10°–16°E. Geochemistry Geophysics Geosystems 3(7), 1-14.

Baudrand, M., Grossi, V., Pancost, R., Aloisi, G., 2010. Non-isoprenoid macrocyclic glycerol diethers associated with authigenic carbonates. Organic Geochemistry 41(12), 1341-1344.

Bennett, S.A., Achterberg, E. P., Connelly, D. P., Statham, P. J., Fones, G. R., German, C. R., 2008. The distribution and stabilisation of dissolved fe in deep-sea hydrothermal plumes. Earth and Planetary Science Letters 270(3–4), 157-167.

Bennett, S.A., Statham, P.J., Green, D.R.H., Le Bris, N., McDermott, J.M., Prado, F., Rouxel, O.J., Von Damm, K., German, C.R., 2011. Dissolved and particulate organic carbon in hydrothermal plumes from the East Pacific Rise, 9°50′N. Deep Sea Research Part I: Oceanographic Research Papers 58(9), 922-931.

Bligh, E., Dyer, W., 1959. A rapid method of total lipid extraction and purification. Canadian Journal of Biochemistry and Physiology 37(8), 911-917.

Blumenberg, M., Seifert, R., Buschmann, B., Kiel, S., Thiel, V., 2012. Biomarkers Reveal Diverse Microbial Communities in Black Smoker Sulfides from Turtle Pits (Mid-Atlantic Ridge, Recent) and Yaman Kasy (Russia, Silurian). Geomicrobiology Journal 29, 66-75.

Blumenberg, M., Seifert, R., Petersen, S., Michaelis, W., 2007. Biosignatures present in a hydrothermal massive sulfide from the Mid-Atlantic Ridge. Geobiology 5(4), 435-450.

Boström, K., Kraemer, T., Gartner, S., 1973. Provenance and accumulation rates of opaline silica, Al, Ti, Fe, Mn, Cu, Ni and Co in Pacific pelagic sediments. Chemical Geology 11(2), 123-148.

Bradley, A.S., Fredricks, H., Hinrichs, K.-U., Summons, R.E., 2009. Structural diversity of diether lipids in carbonate chimneys at the Lost City Hydrothermal Field. Organic Geochemistry 40(12), 1169-1178.

Brassell, S. C., Eglinton, G., Marlowe, I. T., Pflaumann, U., Sarnthein, M., 1986. Molecular stratigraphy: a new tool for climatic assessment. Nature 320(6058), 129-133.

Bray, E.E., Evans, E.D., 1961. Distribution of n-paraffins as a clue to recognition of source beds. Geochimica et Cosmochimica Acta 22(1), 2-15.

Butterfield, D.A., Roe, K.K., Lilley, M.D., Huber, J.A., Baross, J.A., Embley, R.W., Massoth, G.J., 2004. Mixing, Reaction and Microbial Activity in the Sub-Seafloor Revealed by Temporal and Spatial Variation in Diffuse Flow Vents at Axial Volcano. The Subseafloor Biosphere at Mid-Ocean Ridges, 269-289.

Cao, Z., Cao, H., Tao, C., Li, J., Yu, Z., Shu, L., 2012. Rare earth element geochemistry of hydrothermal deposits from Southwest Indian Ridge. Acta Oceanologica Sinica 31(2), 62-69.

Cao, H., Wang, Y., Lee, O.O., Zeng, X., Shao, Z., Qian, P.Y., 2014. Microbial sulfur cycle in two hydrothermal chimneys on the southwest indian ridge. Mbio 5(1), e00980-13.

Cave, R.R., German, C.R., Thomson, J., Nesbitt, R.W., 2002. Fluxes to sediments underlying the Rainbow hydrothermal plume at 36°14′N on the Mid-Atlantic Ridge. Geochimica et Cosmochimica Acta 66(11), 1905–1923.

Chen, Y., Yu, B., Su, X., Yu, M., 2013. Mineralogical and Geochemical Characteristics of the Calcareous Sediments in Southwest Indian Ridge. Geological Science and Technology Information 32, 107–113.

Dai, J., Sun, M.-Y., 2007. Organic matter sources and their use by bacteria in the sediments of the Altamaha estuary during high and low discharge periods. Organic Geochemistry 38(1), 1-15.

De Angelis, M.A., Lilley, M.D., Baross, J.A., 1993. Methane oxidation in deep-sea hydrothermal plumes of the endeavour segment of the Juan de Fuca Ridge. Deep Sea Research Part I Oceanographic Research Papers 40(6), 1169-1186.

De Rosa, M.D., Gambacorta, A., Minale, L., Bu'Lock, J.D., 1971. Bacterial triterpenes. Journal of the Chemical Society D Chemical Communications 12(12), 619-620.

Dias, Á.S., Barriga, F.J.A.S., 2006. Mineralogy and geochemistry of hydrothermal sediments from the serpentinite-hosted Saldanha hydrothermal field (36°34′N; 33°26′W) at MAR. Marine Geology 225(1–4), 157-175.

Dias, A., Mills, R., Taylor, R., Ferreira, P., Barriga, F., 2008. Geochemistry of a sediment push-core from the Lucky Strike hydrothermal field, Mid-Atlantic Ridge. Chemical Geology 247(3), 339-351.

Dick, G.J., Clement, B.G., Webb, S.M., Fodrie, F.J., Bargar, J.R., Tebo, B.M., 2009. Enzymatic

microbial Mn(II) oxidation and Mn biooxide production in the Guaymas Basin deep-sea hydrothermal plume. Geochimica et Cosmochimica Acta 73(21), 6517-6530.

Dick, G.J., Anantharaman, K., Baker, B.J., Li, M., Reed, D.C., Sheik, C.S., 2013. The microbiology of deep-sea hydrothermal vent plumes: ecological and biogeographic linkages to seafloor and water column habitats. Frontiers in Microbiology 4, 124.

Dickson, L., Bull, I.D., Gates, P.J., Evershed, R.P., 2009. A simple modification of a silicic acid lipid fractionation protocol to eliminate free fatty acids from glycolipid and phospholipid fractions. Journal of Microbiological Methods 78(3), 249-54.

Douville, E., Bienvenu, P., Charlou, J.L., Donval, J.P., Fouquet, Y., Appriou, P., Gamo, T., 1999. Yttrium and rare earth elements in fluids from various deep-sea hydrothermal systems. Geochimica et Cosmochimica Acta 63(5), 627-643.

Edwards, K.J., Glazer, B.T., Rouxel, O.J., Bach, W., Emerson, D., Davis, R.E., Toner, B.M., Chan, C.S., Tebo, B.M., Staudigel, H., Moyer, C.L., 2011. Ultra-diffuse hydrothermal venting supports Fe-oxidizing bacteria and massive umber deposition at 5000 m off Hawaii. ISME Journal 5(11), 1748-58.

Eglinton, G., Hamilton, R.J., 1967. Leaf epicuticular waxes. Science 156(3780), 1322-1335.

Elderfield, H., Schultz, A., 1996. Mid-ocean ridge hydrothermal fluxes and the chemical composition of the ocean. Annual Review of Earth and Planetary Sciences 24, 191-214.

Elvert, M., Hopmans, E.C., Treude, T., Boetius, A., Suess, E., 2005. Spatial variations of methanotrophic consortia at cold methane seeps: implications from a high-resolution molecular and isotopic approach. Geobiology 3(3), 195-209.

Estapa, M.L., Breier, J.A., German, C.R., 2015. Particle dynamics in the rising plume at Piccard Hydrothermal Field, Mid-Cayman Rise. Geochemistry, Geophysics, Geosystems 16(8), 2762-2774.

Farrimond, P., Innes, H.E., Head, I.M., 2000. Environmental influence on the biohopanoid composition of recent sediments. Geochimica et Cosmochimica Acta 64(17), 2985-2992.

Fietz, S., Prahl, F.G., Moraleda, N., Rosell-Melé, A., 2013. Eolian transport of glycerol dialkyl glycerol tetraethers (GDGTs) off Northwest Africa. Organic Geochemistry 64, 112-118.

Fitzsimmons, J.N., Boyle, E.A., Jenkins, W.J., 2014. Distal transport of dissolved hydrothermal iron in the deep South Pacific Ocean. Proceedings of the National Academy of Sciences of the United States of America 111(47), 16654-61.

Fitzsimmons, J.N., John, S.G., Marsay, C.M., Hoffman, C.L., Nicholas, S.L., Toner, B.M., German, C.R., Sherrell, R.M., 2017. Iron persistence in a distal hydrothermal plume supported by dissolved-particulate exchange. Nature Geoscience 10, 195-201.

Fujimoto, H. et al., 1999. First submersible investigations of mid-ocean ridges in the Indian Ocean. InterRidge News 8, 22-24.

Gao, C., Dick, H.J.B., Liu, Y., Zhou, H., 2016. Melt extraction and mantle source at a Southwest Indian Ridge Dragon Bone amagmatic segment on the Marion Rise. Lithos 246, 48-60.

German, C.R., 2003. Hydrothermal activity on the eastern SWIR (50°-70°E): Evidence from core-top geochemistry, 1887 and 1998. Geochemistry Geophysics Geosystems 4(7), 9103.

German, C.R., Hergt, J., Palmer, M.R., Edmond, J.M., 1999. Geochemistry of a hydrothermal sediment core from the OBS vent-field, 21°N East Pacific Rise. Chemical Geology 155(1), 65-75.

German, C.R., Higgs, N.C., Thomson, J., Mills, R., Elderfield, H., Blusztajn, J., Fleer, A.P., Bacon, M.P., 1993. A geochemical study of metalliferous sediment from the TAG Hydrothermal

Mound, 26°08′N, Mid-Atlantic Ridge. Journal of Geophysical Research Atmospheres 98(B6), 9683-9692.

German, C.R., Klinkhammer, G.P., Edmond, J.M., Mura, A., Elderfield, H., 1990. Hydrothermal scavenging of rare-earth elements in the ocean. Nature 345(6275), 516-518.

German, C.R., Legendre, L.L., Sander, S.G., Niquil, N., Luther III, G.W., Bharati, L., Han, X., Le Bris, N., 2015. Hydrothermal Fe cycling and deep ocean organic carbon scavenging: Model-based evidence for significant POC supply to seafloor sediments. Earth and Planetary Science Letters 419, 143-153.

Gibson, R.A., van der Meer, M.T.J., Hopmans, E.C., Reysenbach, A.L., Schouten, S., Sinninghe Damsté, J.S., 2013. Comparison of intact polar lipid with microbial community composition of vent deposits of the Rainbow and Lucky Strike hydrothermal fields. Geobiology 11(1), 72-85.

Goad, L.J., Goodwin, T.W., 1972. The biosynthesis of plant sterols. Progress in Phytochemistry 3, 113 -198.

He, B., Xu, Y.G., Zhong, Y.T., Guan, J.P., 2010. The Guadalupian–Lopingian boundary mudstones at Chaotian (SW China) are clastic rocks rather than acidic tuffs: Implication for a temporal coincidence between the end-Guadalupian mass extinction and the Emeishan volcanism. Lithos 119(1–2), 10-19.

Huang, X., Zeng, Z., Chen, S., Yin, X., Wang, X., Zhao, H., Yang, B., Rong, K., Ma, Y., 2014. Component characteristics of organic matter in hydrothermal barnacle shells from Southwest Indian Ridge. Acta Oceanologica Sinica 32(12), 60-67.

Huber, R., Rossnagel, P., Woese, C.R., Rachel, R., Langworthy, T.A., Stetter, K.O., 1996. Formation of ammonium from nitrate during chemolithoautotrophic growth of the extremely thermophilic bacterium ammonifex degensii gen. nov. sp. nov. Systematic and Applied Microbiology 19(1), 40-49.

Huber, R., Wilharm, T., Huber, D., Trincone, A., Burggraf, S., König, H., Reinhard, R., Rockinger, R., Fricke, H., Stetter, K.O., 1992. Aquifex pyrophilus gen. nov. sp. nov., represents a novel group of marine hyperthermophilic hydrogen-oxidizing bacteria. Systematic and Applied Microbiology 15(3), 340-351.

Jaeschke, A., Eickmann, B., Lang, S.Q., Bernasconi, S.M., Strauss, H., Frühgreen, G.L., 2014. Biosignatures in chimney structures and sediment from the Loki's Castle low-temperature hydrothermal vent field at the Arctic Mid-Ocean Ridge. Extremophiles 18(3), 545-60.

Jaeschke, A., Jørgensen, S.L., Bernasconi, S.M., Pedersen, R.B., Thorseth, I.H., Früh-Green, G.L., 2012. Microbial diversity of Loki's Castle black smokers at the Arctic Mid-Ocean Ridge. Geobiology 10(6), 548-561.

Jahnke, L.L., Eder, W., Huber, R., Hope, J.M., Hinrichs, K.U., Hayes, J.M., Des Marais, D.J., Cady, S.L., Summons, R.E., 2001. Signature Lipids and Stable Carbon Isotope Analyses of Octopus Spring Hyperthermophilic Communities Compared with Those ofAquificales Representatives. Applied and Environmental Microbiology 67(11), 5179-5189.

Kato, S., Takano, Y., Kakegawa, T., Oba, H., Inoue, K., Kobayashi, C., Utsumi, M., Marumo, K., Kobayashi, K., Ito, Y., Ishibashi, J., Yamagishi, A., 2010. Biogeography and biodiversity in sulfide structures of active and inactive vents at deep-sea hydrothermal fields of the Southern Mariana Trough. Applied and Environmental Microbiology 76(9), 2968-79.

Kaur, G., Mountain, B.W., Hopmans, E.C., Pancost, R.D., 2011. Preservation of microbial lipids in

geothermal sinters. Astrobiology 11(3), 259-74.

Kaur, G., Mountain, B.W., Pancost, R.D., 2008. Microbial membrane lipids in active and inactive sinters from Champagne Pool, New Zealand: Elucidating past geothermal chemistry and microbiology. Organic Geochemistry 39(8), 1024-1028.

Kaur, G., Mountain, B.W., Stott, M.B., Hopmans, E.C., Pancost, R.D., 2015. Temperature and pH control on lipid composition of silica sinters from diverse hot springs in the Taupo Volcanic Zone, New Zealand. Extremophiles 19(2), 327-344.

Kim, J.-H., Crosta, X., Michel, E., Schouten, S., Duprat, J., Sinninghe Damsté, J. S., 2009. Impact of lateral transport on organic proxies in the Southern Ocean. Quaternary Research 71(2), 246-250.

Kleint, C., Hawkes, J.A., Sander, S.G., Koschinsky, A., 2016. Voltammetric investigation of hydrothermal iron speciation. Frontiers in Marine Science 3. https://doi.org/10.3389/fmars.2016.00075.

Konn, C., Testemale, D., Querellou, J., Holm, N.G., Charlou, J.L., 2011. New insight into the contributions of thermogenic processes and biogenic sources to the generation of organic compounds in hydrothermal fluids. Geobiology 9(1), 79-93.

Lam, P., Cowen, J.P., Jones, R.D., 2004. Autotrophic ammonia oxidation in a deep-sea hydrothermal plume. FEMS Microbiology Ecology 47(2), 191-206.

Lang, S.Q., Butterfield, D.A., Lilley, M.D., Johnson, H.P., Hedges, J.I., 2006. Dissolved organic carbon in ridge-axis and ridge-flank hydrothermal systems. Geochimica et Cosmochimica Acta 70(15), 3830-3842.

Langworthy, T.A., Holzer, G., Zeikus, J.G., Tornabene, T.G., 1983. Iso-and anteiso-branched glycerol diethers of the thermophilic anaerobe Thermodesulfotobacterium commune. Systematic and Applied Microbiology 4(1), 1-17.

Lei, J., Chu, F., Yu, X., Li, X., Tao, C., Ge, Q., 2015. Composition and genesis implications of hydrocarbons in 49.6°E hydrothermal area, Southwest Indian Ocean Ridge. Earth Science Frontiers 22(1), 281-290.

Lesniewski, R.A., Jain, S., Anantharaman, K., Schloss, P.D., Dick, G.J., 2012. The metatranscriptome of a deep-sea hydrothermal plume is dominated by water column methanotrophs and lithotrophs. ISME Journal 6(12), 2257-68.

Li, J., Zhou, H., Peng, X., Wu, Z., Chen, S., Fang, J., 2012. Microbial diversity and biomineralization in low-temperature hydrothermal iron-silica-rich precipitates of the Lau Basin hydrothermal field. FEMS Microbiology Ecology 81(1), 205-16.

Li, J., Peng, X., Zhou, H., Li, J., Sun, Z., 2013. Molecular evidence for microorganisms participating in Fe, Mn, and S biogeochemical cycling in two low-temperature hydrothermal fields at the Southwest Indian Ridge. Journal of Geophysical Research: Biogeosciences 118(2), 665-679.

Li, M., Baker, B. J., Anantharaman, K., Jain, S., Breier, J.A., Dick, G.J., 2015. Genomic and transcriptomic evidence for scavenging of diverse organic compounds by widespread deep-sea archaea. Nature Communications 6, 8933.

Li, J., Zhou, H., Fang, J., Wu, Z., Peng, X., 2016a. Microbial Distribution in a Hydrothermal Plume of the Southwestern Indian Ridge. Geomicrobiology Journal 33(5), 401-415.

Li, Z., Chu, F., Jin, L., Li, X., Dong, Y., Chen, L., Zhu, J., 2016b. Major and trace element composition of surface sediments from the Southwest Indian Ridge: evidence for the incorporation of a hydrothermal component. Acta Oceanologica Sinica 35(2), 101-108.

Littke, R., Rullkötter, J., Schaefer, R.G., 1991. Organic and carbonate carbon accumulation on Broken Ridge and Ninetyeast Ridge, Central Indian Ocean. Cardiologia 36(1), 23-9.

Luo, A., 2016. Geological and geochemical characteristics of an inactive hydrothermal chimney from Longqi Field, Southwest Indian Ridge (M.Sc. dissertation). Tongji University, China.

Münch, U., Lalou, C., Halbach, P., Fujimoto, H., 2001. Relict hydrothermal events along the super-slow Southwest Indian spreading ridge near 63°56′E—mineralogy, chemistry and chronology of sulfide samples. Chemical Geology 177(3–4), 341-349.

Mccarthy, M.D., Beaupré, S.R., Walker, B.D., Voparil, I., Guilderson, T.P., Druffel, E.R.M., 2011. Chemosynthetic origin of ^{14}C-depleted dissolved organic matter in a ridge-flank hydrothermal system. Nature Geoscience 4(1), 32-36.

Mccollom, T.M., 2000. Geochemical constraints on primary productivity in submarine hydrothermal vent plumes. Deep Sea Research Part I Oceanographic Research Papers 47(1), 85-101.

Metz, S., Trefry, J.H., Nelsen, T.A., 1988. History and geochemistry of a metalliferous sediment core from the Mid-Atlantic Ridge at 26°N. Geochimica et Cosmochimica Acta 52(10), 2369-2378.

Meyers, P.A., 1997. Organic geochemical proxies of paleoceanographic, paleolimnologic, and paleoclimatic processes. Organic Geochemistry 27, 213-250.

Mille, G., Asia, L., Guiliano, M., Malleret, L., Doumenq, P., 2007. Hydrocarbons in coastal sediments from the Mediterranean sea (Gulf of Fos area, France). Marine Pollution Bulletin 54(5), 566-575.

Mills, R.A., Elderfield, H., 1995. Hydrothermal activity and the geochemistry of metalliferous sediment. Seafloor hydrothermal systems: physical, chemical, biological, and geological interactions: 392-407.

Niemann, H., Elvert, M., 2008. Diagnostic lipid biomarker and stable carbon isotope signatures of microbial communities mediating the anaerobic oxidation of methane with sulphate. Organic Geochemistry 39(12), 1668-1677.

Nishimura, M., Baker, E.W., 1986. Possible origin of n-alkanes with a remarkable even-to-odd predominance in recent marine sediments. Geochimica et Cosmochimica Acta 50(2), 299-305.

Noll, P.D., Newsom, H.E., Leeman, W.P., Ryan, J.G., 1996. The role of hydrothermal fluids in the production of subduction zone magmas: Evidence from siderophile and chalcophile trace elements and boron. Geochimica et Cosmochimica Acta 60(4), 587-611.

Oba, M., Sakata, S., Tsunogai, U., 2006. Polar and neutral isopranyl glycerol ether lipids as biomarkers of archaea in near-surface sediments from the Nankai Trough. Organic Geochemistry 37(12), 1643-1654.

Pan, A., Yang, Q., Zhou, H., Ji, F., Wang, H., Pancost, R.D., 2016. A diagnostic GDGT signature for the impact of hydrothermal activity on surface deposits at the Southwest Indian Ridge. Organic Geochemistry 99, 90-101.

Pancost, R.D., Sinninghe Damsté, J.S., De Lint, S., van der Maarel, M.J.E.C., Gottschal, J.C., Medinaut Shipboard Scientific Party, 2000. Biomarker evidence for widespread anaerobic methane oxidation in Mediterranean sediments by a consortium of methanogenic archaea and bacteria. Applied and Environmental Microbiology 66(3), 1126.

Pancost, R.D., Hopmans, E.C., Sinninghe Damsté, J.S., Medinauth Scientific Party, 2001. Archaeal lipids in Mediterranean cold seeps: molecular proxies for anaerobic methane oxidation. Geochimica et Cosmochimica Acta 65(10), 1611-1627.

Pancost, R.D., Pressley, S., Coleman, J.M., Benning, L.G., Mountain, B.W., 2005. Lipid biomolecules

in silica sinters: indicators of microbial biodiversity. Environmental Microbiology 7(1), 66-77.

Pancost, R.D., Pressley, S., Coleman, J.M., Talbot, H.M., Kelly, S. P., Farrimond, P., Schouten, S., Benning, L.G., Mountain, B.W., 2006. Composition and implications of diverse lipids in New Zealand geothermal sinters. Geobiology 4, 71-92.

Peng, X., Chen, S., Zhou, H., Zhang, L., Wu, Z., Li, J., Li, J., Xu, H., 2011. Diversity of biogenic minerals in low-temperature Si-rich deposits from a newly discovered hydrothermal field on the ultraslow spreading Southwest Indian Ridge. Journal of Geophysical Research 116, G03030. http://dx.doi.org/10.1029/2011JG001691.

Peng, X., Li, J., Zhou, H., Wu, Z., Li, J., Chen, S., Yao, H., 2011b. Characteristics and source of inorganic and organic compounds in the sediments from two hydrothermal fields of the Central Indian and Mid-Atlantic Ridges. Journal of Asian Earth Sciences 41(3), 355-368.

Perner, M., Seifert, R., Weber, S., Koschinsky, A., Schmidt, K., Strauss, H., Peters, M., Haase, K., Imhoff, J.F., 2007. Microbial CO_2 fixation and sulfur cycling associated with low-temperature emissions at the Lilliput hydrothermal field, southern Mid-Atlantic Ridge (9°S). Environmental Microbiology 9(5), 1186-201.

Petersen, J.M., Zielinski, F.U., Pape, T., Seifert, R., Moraru, C., Amann, R., Hourdez, S., Girguis, P.R., Wankel, S.D., Barbe, V., Pelletier, E., Fink, D., Borowski, C., Bach, W., Dubilier, N., 2011. Hydrogen is an energy source for hydrothermal vent symbioses. Nature 476(7359), 176-180.

Pitcher, A., Hopmans, E.C., Schouten, S., Sinninghe Damsté, J.S., 2009. Separation of core and intact polar archaeal tetraether lipids using silica columns: Insights into living and fossil biomass contributions. Organic Geochemistry 40(1), 12-19.

Poynter, J.G., Farrimond, P., Brassell, S.C., Eglinton, G., 1989. Aeolian-derived higherplant lipids in the marine sedimentary record: Links with paleoclimate. In: Leinen, M., Sarnthein, M. (Eds.), Palaeoclimatology and Palaeometeorology: Modern and Past Patterns of Global Atmosphere Transport. Kluwer, pp. 435–462.

Reeves, E.P., Yoshinaga, M.Y., Pjevac, P., Goldenstein, N.I., Peplies, J., Meyerdierks, A., Amann, R., Bach, W., Hinrichs, K.-U., 2014. Microbial lipids reveal carbon assimilation patterns on hydrothermal sulfide chimneys. Environmental Microbiology 16(11), 3515-32.

Resing, J.A., Sedwick, P.N., German, C.R., Jenkins, W.J., Moffett, J.W., Sohst, B.M., Tagliabue, A., 2015. Basin-scale transport of hydrothermal dissolved metals across the South Pacific Ocean. Nature 523(7559), 200-3.

Rohmer, M., Bouvier-Nave, P., Ourisson, G., 1984. Distribution of Hopanoid Triterpenes in Prokaryotes. Microbiology 130(5), 1137-1150.

Ruhlin, D.E., Owen, R.M., 1986. The rare earth element geochemistry of hydrothermal sediments from the East Pacific Rise: Examination of a seawater scavenging mechanism. Geochimica et Cosmochimica Acta 50(3), 393-400.

Rushdi, A.I., Simoneit, B.R.T., 2002. Hydrothermal alteration of organic matter in sediments of the Northeastern Pacific Ocean: Part 1. Middle Valley, Juan de Fuca Ridge. Applied Geochemistry 17(11), 1401-1428.

Rütters, H., Sass, H., Cypionka, H., Rullkotter, J., 2001. Monoalkylether phospholipids in the sulfate-reducing bacteria Desulfosarcina variabilis and Desulforhabdus amnigenus. Arch Microbiol 176(6), 435-42.

Sander, S.G., Koschinsky, A., 2016. The export of iron and other trace metals from hydrothermal vents and the impact on their marine biogeochemical Cycle. Trace Metal Biogeochemistry and

Ecology of Deep-Sea Hydrothermal Vent Systems in The Handbook of Environmental Chemistry 50, 9-24.

Sands, C.M., Connelly, D.P., Statham, P.J., German, C.R., 2012. Size fractionation of trace metals in the Edmond hydrothermal plume, Central Indian Ocean. Earth and Planetary Science Letters s 319–320, 15-22.

Schmidt, K., Koschinsky, A., Garbe-Schönberg, D., Carvalho, L.M.D., Seifert, R., 2007. Geochemistry of hydrothermal fluids from the ultramafic-hosted Logatchev hydrothermal field, 15°N on the Mid-Atlantic Ridge: Temporal and spatial investigation. Chemical Geology 242(1–2), 1-21.

Schouten, S., Hopmans, E.C., Schefuβ, E., Sinninghe Damsté, J.S., 2002. Distributional variations in marine crenarchaeotal membrane lipids a new organic proxy for reconstructing ancient sea water temperatures. Earth and Planetary Science Letters 204, 265-274.

Schouten, S., Wakeham, S.G., Hopmans, E.C., Sinninghe Damsté, J.S., 2003. Biogeochemical evidence that thermophilic archaea mediate the anaerobic oxidation of methane. Applied and Environmental Microbiology 69(3), 1680-6.

Schouten, S., Hopmans, E.C., Sinninghe Damsté, J.S., 2013. The organic geochemistry of glycerol dialkyl glycerol tetraether lipids: a review. Organic Geochemistry 54, 19–61.

Seifert, W.K., Moldowan, J.M., 1978. Applications of steranes, terpanes and monoaromatics to the maturation, migration and source of crude oils. Geochimica et Cosmochimica Acta 42(1), 77-95.

Sheik, C.S., Anantharaman, K., Breier, J.A., Sylvan, J.B., Edwards, K.J., Dick, G., 2015. Spatially resolved sampling reveals dynamic microbial communities in rising hydrothermal plumes across a back-arc basin. ISME Journal 9(6), 1434-1445.

Shulga, N.A., Peresypkin, V.I., Revelskii, I.A., 2010. Composition research of n-alkanes in the samples of hydrothermal deposits of the Mid-Atlantic Ridge by means of gas chromatography-mass spectrometry. Oceanology 50(4), 479-487.

Shulga, N.A., Peresypkin, V.I., 2012. The genesis of hydrocarbons in hydrothermal deposits of the lost city and rainbow fields (Mid-Atlantic Ridge). Doklady Earth Sciences 445(1), 879-882.

Simoneit, B.R.T., Lein, A.Y., Peresypkin, V.I., Osipov, G.A., 2004. Composition and origin of hydrothermal petroleum and associated lipids in the sulfide deposits of the Rainbow field (Mid-Atlantic Ridge at 36°N). Geochimica et Cosmochimica Acta 68(10), 2275-2294.

Sinninghe Damsté, J.S., Rijpstra, W.I.C., Reichart, G.J., 2002. The influence of oxic degradation on the sedimentary biomarker record II. Evidence from Arabian Sea sediments. Geochimica et Cosmochimica Acta 66(15), 2737-2754.

Slack, J.F., Grenne, T., Bekker, A., 2009. Seafloor-hydrothermal Si-Fe-Mn exhalites in the Pecos greenstone belt, New Mexico, and the redox state of ca. 1720 Ma deep seawater. Geosphere 5(3), 302-314.

Sun, Z., Zhou, H., Yang, Q., Sun, Z., Bao, S., Yao, H., 2011. Hydrothermal Fe–Si–Mn oxide deposits from the Central and South Valu Fa Ridge, Lau Basin. Applied Geochemistry 26(7), 1192-1204.

Sun, Z., Zhou, H., Glasby, G.P., Yang, Q., Yin, X., Li, J., Chen, Z., 2012. Formation of Fe–Mn–Si oxide and nontronite deposits in hydrothermal fields on the Valu Fa Ridge, Lau Basin. Journal of Asian Earth Sciences 43(1), 64-76.

Sun, Z., Zhou, H., Glasby, G.P., Sun, Z., Yang, Q., Yin, X., Li, J., 2013. Mineralogical characterization and formation of Fe-Si oxyhydroxide deposits from modern seafloor hydrothermal vents.

American Mineralogist 98(1), 85-97.

Sun, Z., Li, J., Huang, W., Dong, H., Little, C.T.S., Li, J., 2015. Generation of hydrothermal Fe-Si oxyhydroxide deposit on the Southwest Indian Ridge and its implication for the origin of ancient banded iron formations. Journal of Geophysical Research Biogeosciences 120(1), 187-203.

Sylvan, J.B., Pyenson, B.C., Rouxel, O., German, C.R., Edwards, K.J., 2012. Time-series analysis of two hydrothermal plumes at 9°50'N East Pacific Rise reveals distinct, heterogeneous bacterial populations. Geobiology 10(2), 178-92.

Tao, C., Lin, J., Guo, S., Chen, Y., Wu, G., Han, X., German, C., Yoerger, D., Zhu, J., Zhou, N., 2007. The Chinese DY115-19 Cruise: Discovery of the first active hydrothermal vent field at the ultraslow spreading Southwest Indian Ridge. InterRidge News 16, 25-26.

Tao, C., Li, H., Huang, W., Han, X., Wu, G., Su, X., Zhou, N., Lin, J., He, Y., Zhou, J., 2011. Mineralogical and geochemical features of sulfide chimneys from the 49°39′ E hydrothermal field on the Southwest Indian Ridge and their geological inferences. Chinese Science Bulletin 56(26), 2828-2838.

Tao, C., Lin, J., Guo, S., Chen, Y.J., Wu, G., Han, X., German, C.R., Yoerger, D.R., Zhou, N., Li, H., Su, X., Zhu, J., 2012. First active hydrothermal vents on an ultraslow-spreading center: Southwest Indian Ridge. Geology 40(1), 47-50.

Toner, B.M., Marcus, M.A., Edwards, K.J., Rouxel, O., 2012. Measuring the Form of Iron in Hydrothermal Plume Particles. Oceanography 25(1), 209-212.

Van Andel, T.H., 1975. Mesozoic/cenozoic calcite compensation depth and the global distribution of calcareous sediments. Earth and Planetary Science Letters 26(2), 187-194.

Volkman, J. K., 1986. A review of sterol markers for marine and terrigenous organic matter. Organic Geochemistry 9(2), 83-99.

Wang, X., Chen, Y., Lei, J., Wu, M., Zhao, Y., 1982. REE geochemistry in sea-floor sediments in the continental shelf of East China Sea. Geochimica 1, 56-65.

Figures:

Fig. 1. Station location map at the Southwest Indian Ridge (after Pan et al., 2016). Locations are shown for (a) most background sediments (yellow circles) and (b) the far-field metalliferous sediments (M-T1, white triangles), near-field metalliferous sediments (M-T2 and M-T3, blue and red triangles, respectively), and low-temperature hydrothermal deposits (green squares).

Fig. 2. Ternary diagram of Fe, Cu×100 and Ca in samples collected from the SWIR. All samples were divided into three main categories including background sediments, metalliferous sediments and low-temperature hydrothermal deposits.

The type of metalliferous sediments can be further divided into M-T1, M-T2 and M-T3. Note the hydrothermally sourced elements (Fe and Cu) enriched in metalliferous sediments and hydrothermal deposits; whereas background sediments are enriched in calcium. The data of high-temperature sulfides from the SWIR were cited from Luo, 2016.

Fig. 3. Concentrations of elements in metalliferous sediments, including M-T1 (Panel a), M-T2 (Panel b), M-T3 (Panel c), and hydrothermal deposits (Panel d), normalized to average concentrations of the background sediments from the SWIR (hereafter SWA).

Fig. 4. North American shale composite-normalized rare earth element (REE) distribution patterns of background sediments (Panel a), M-T1 (Panel b), M-T2 (Panel c), M-T3 (Panel d) and hydrothermal deposits (Panel e) from the SWIR. Data for seawater, hydrothermal fluid and pelagic sediment are from Douville et al. (1999), Schmidt et al. (2007) and Wang et al. (1982), respectively.

Fig. 5. The distribution of free fatty acids, glycolipid fatty acids and phospholipid fatty acids in background sediments and M-T1 sediments from the SWIR. SFAs, BrFAs and MUFAs represent saturated fatty acids, branched fatty acids and monounsaturated fatty acids, respectively. Other SFAs: C_{10}–C_{15}+C_{17}–C_{32}; other BrFAs: brC_{14}, brC_{18}, brC_{19}; other MUFAs: $C_{14:1}$, $C_{17:1}$, $C_{19:1}$, $C_{20:1}$, $C_{24:1}$.

Fig. 6. Crossplots of Al/(Al+Fe+Mn) versus Fe/Ti for all deposits from the SWIR. The curved line (Slack et al., 2009) represents the ideal mixing between Al-free hydrothermal sediment and pelagic or terrigenous sediment. The data on the left

of the figure, with lower Al/(Al+Fe+Mn) and higher Fe/Ti, could represent the hydrothermal end-member. The dotted line shows the Al/(Al+Fe+Mn) boundary between normal pelagic sediment and samples closer to hydrothermal structures (Boström, 1973).

Appendix 1. Chemical structures cited in the text.

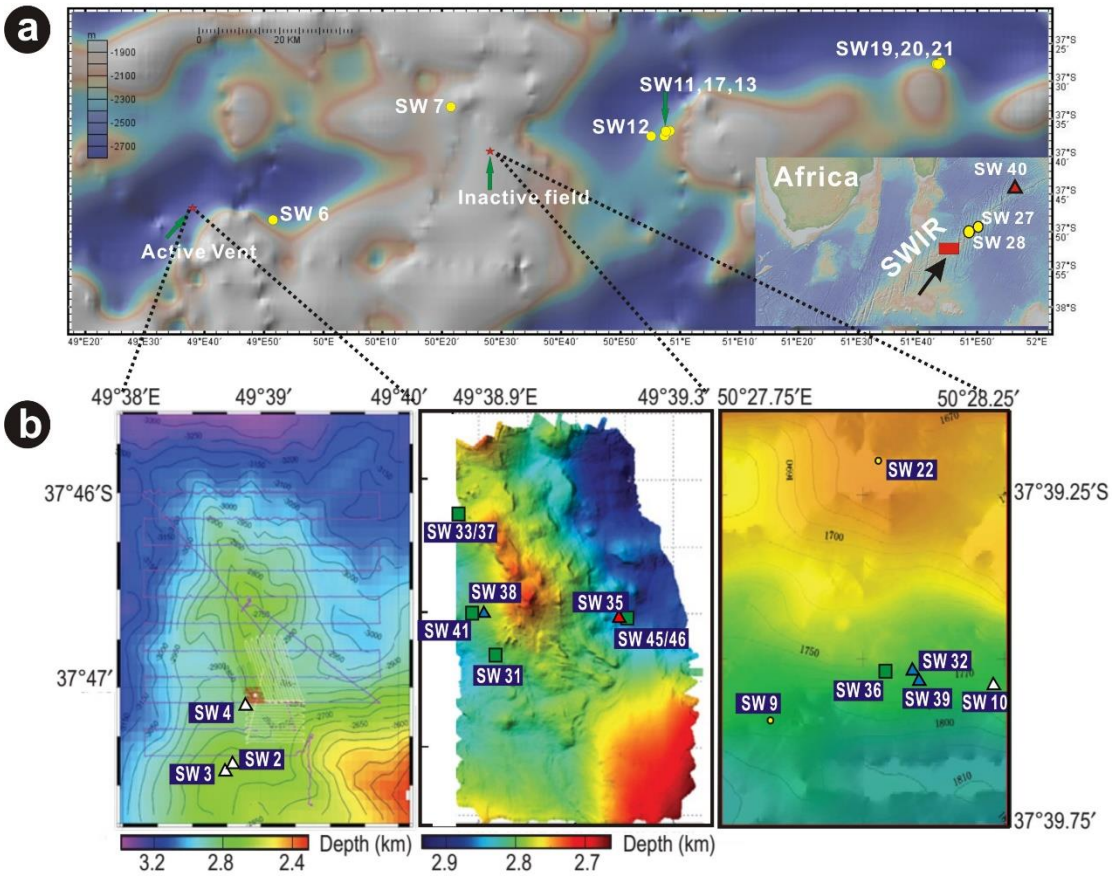

Fig. 1.

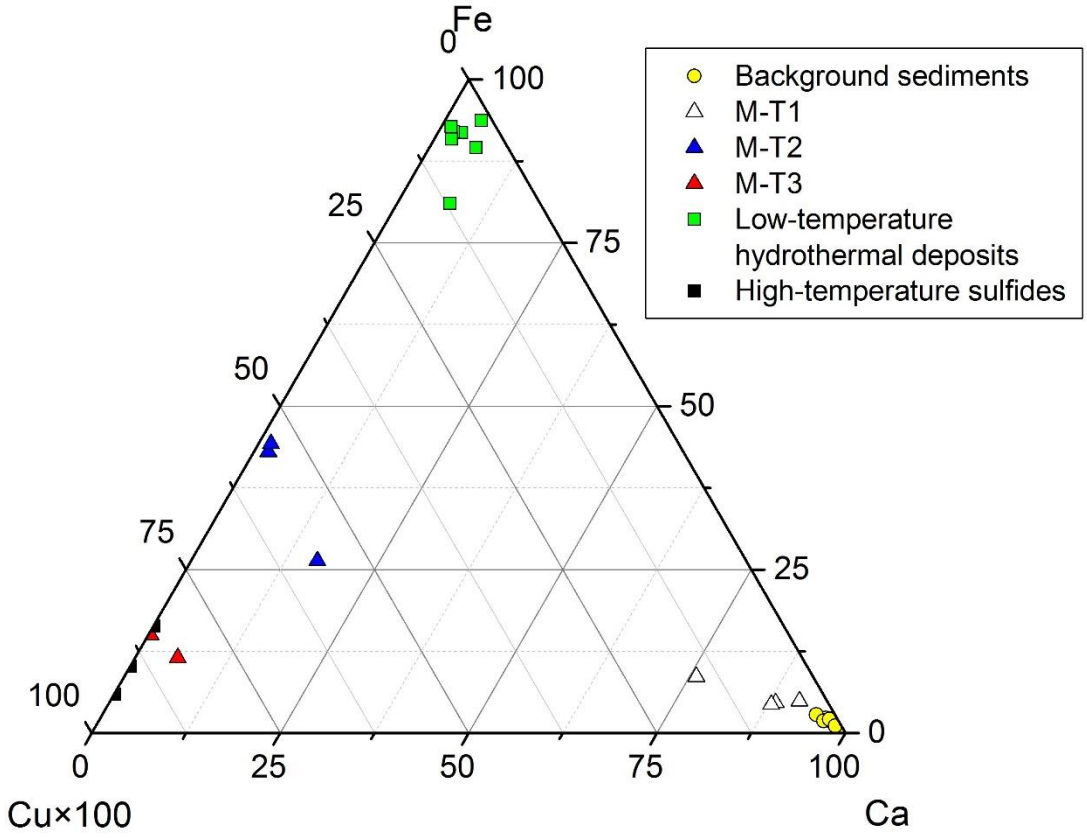
Fe
0
100
25
75
50
50
75
25
100
0
0
25
50
75
100
Cu×100
Ca
Background sediments
M-T1
M-T2
M-T3
Low-temperature hydrothermal deposits
High-temperature sulfides

Fig. 2.

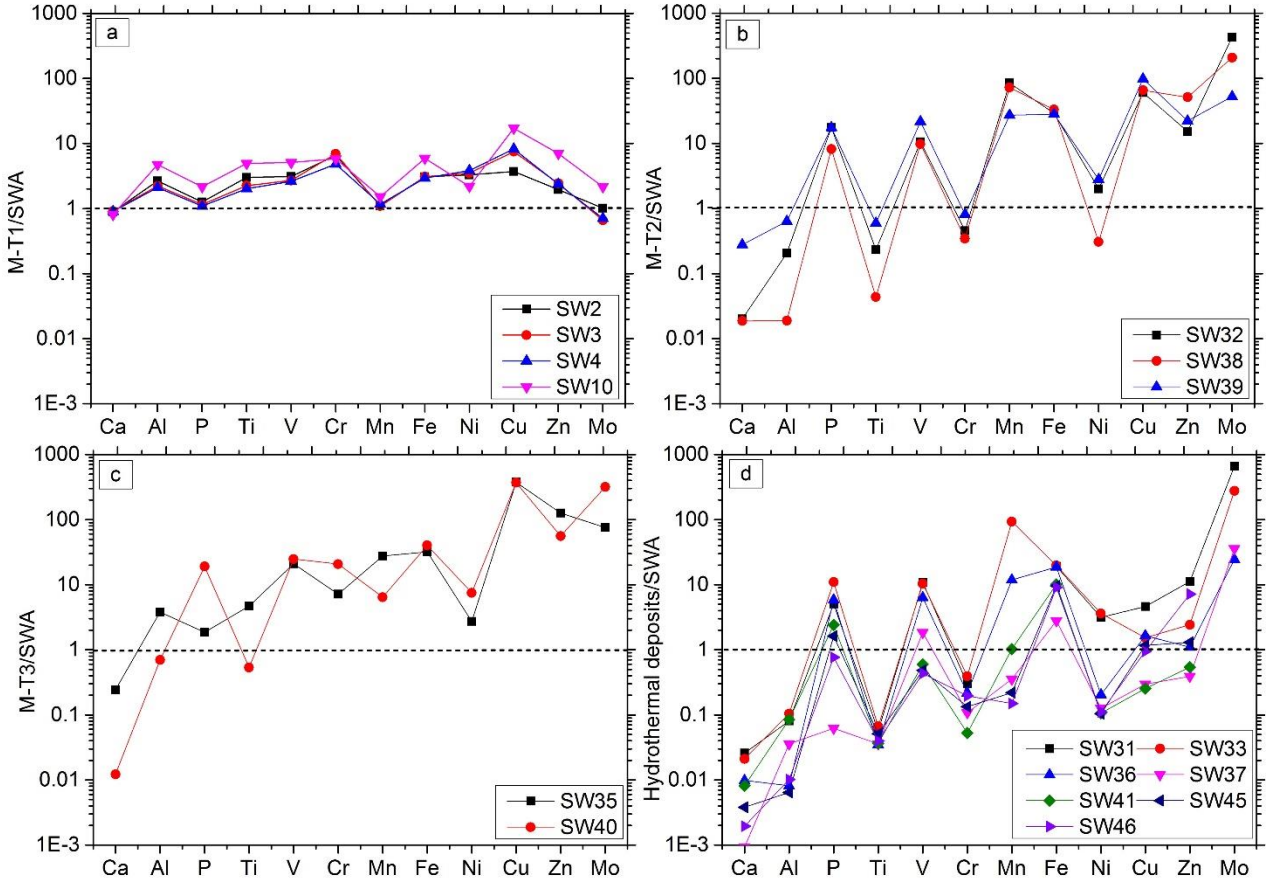
a
b
c
d
M-T1/SWA
M-T2/SWA
M-T3/SWA
Hydrothermal deposits/SWA
1000
100
10
1
0.1
0.01
1E-3
Ca Al P Ti V Cr Mn Fe Ni Cu Zn Mo
SW2
SW3
SW4
SW10
SW32
SW38
SW39
SW35
SW40
SW31
SW33
SW36
SW37
SW41
SW45
SW46

Fig. 3.

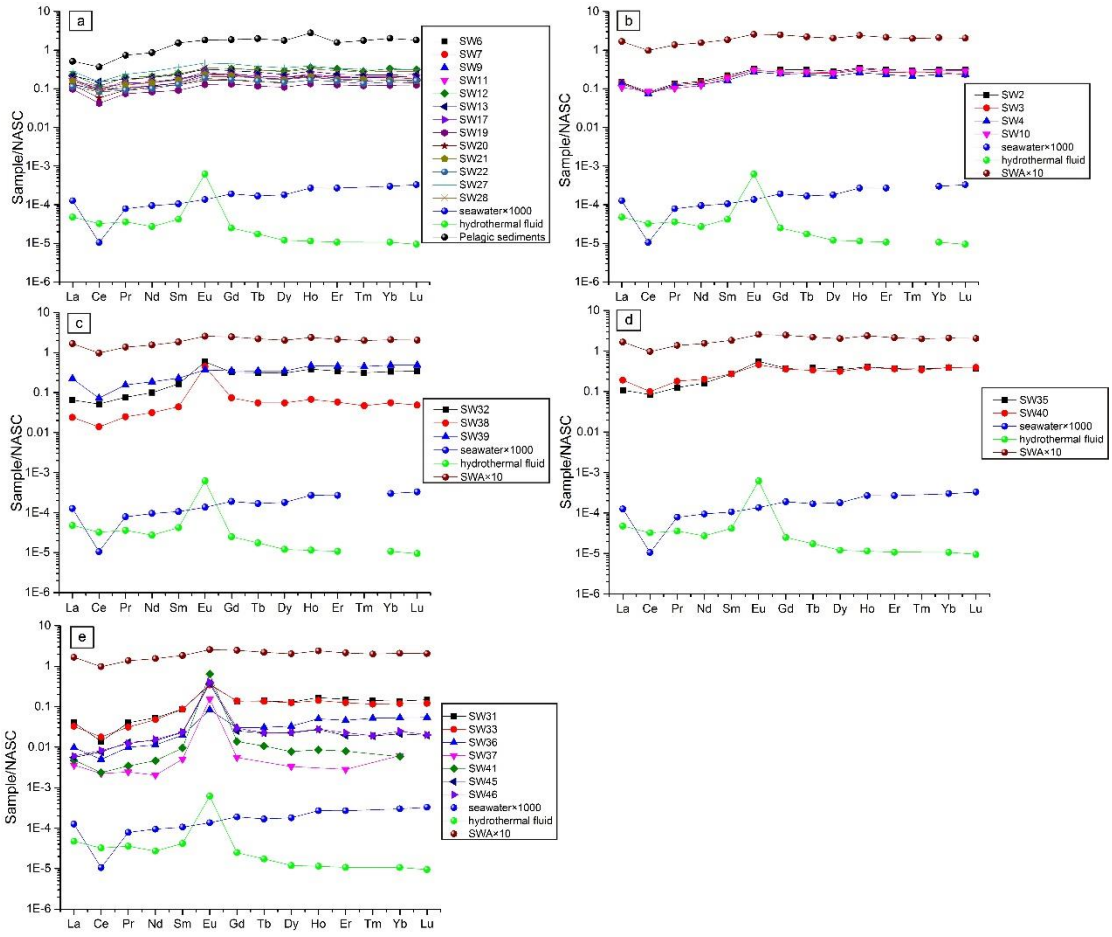
a
SW6
SW7
SW9
SW11
SW12
SW13
SW17
SW19
SW20
SW21
SW22
SW27
SW28
seawater×1000
hydrothermal fluid
Pelagic sediments
b
SW2
SW3
SW4
SW10
seawater×1000
hydrothermal fluid
SWA×10
c
SW32
SW38
SW39
seawater×1000
hydrothermal fluid
SWA×10
d
SW35
SW40
seawater×1000
hydrothermal fluid
SWA×10
e
SW31
SW33
SW36
SW37
SW41
SW45
SW46
seawater×1000
hydrothermal fluid
SWA×10
Sample/NASC
La Ce Pr Nd Sm Eu Gd Tb Dy Ho Er Tm Yb Lu

Fig. 4.

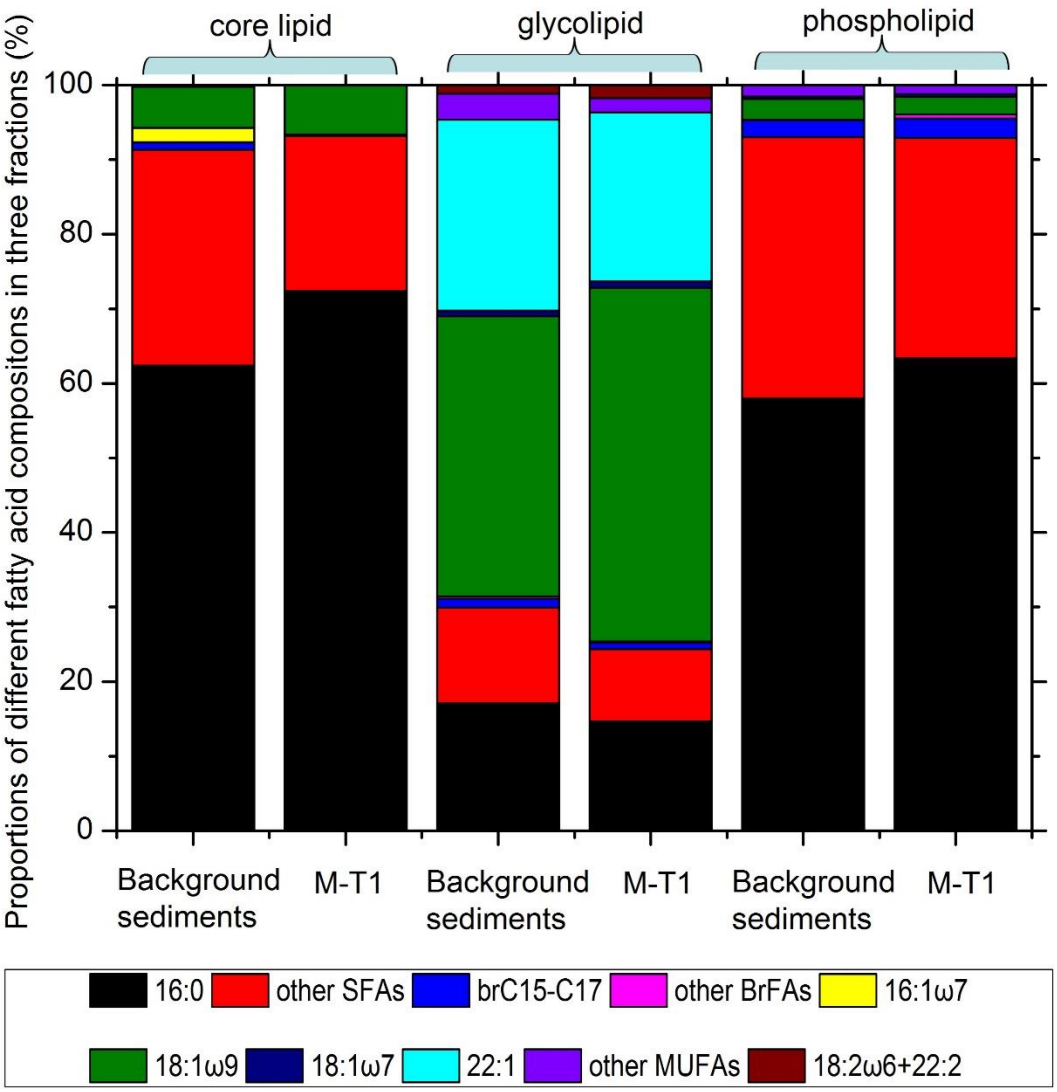
core lipid
glycolipid
phospholipid
Proportions of different fatty acid compositons in three fractions (%)
100
80
60
40
20
0
Background sediments
M-T1
Background sediments
M-T1
Background sediments
M-T1
16:0
other SFAs
brC15-C17
other BrFAs
16:1ω7
18:1ω9
18:1ω7
22:1
other MUFAs
18:2ω6+22:2

Fig. 5.

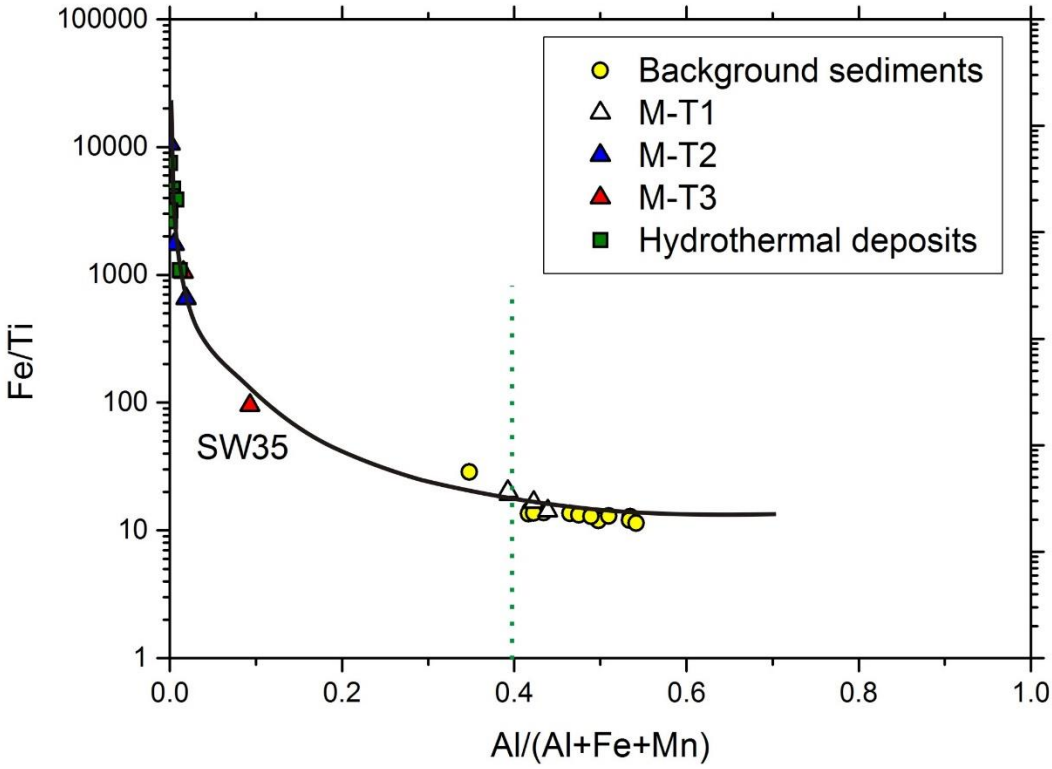
Background sediments
M-T1
M-T2
M-T3
Hydrothermal deposits
SW35
Fe/Ti
Al/(Al+Fe+Mn)
100000
10000
1000
100
10
1
0.0
0.2
0.4
0.6
0.8
1.0

Fig. 6.

Appendix

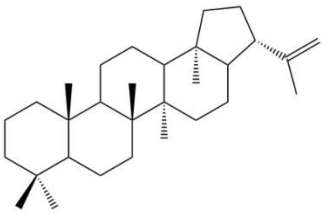

Ⅰ. Diploptene

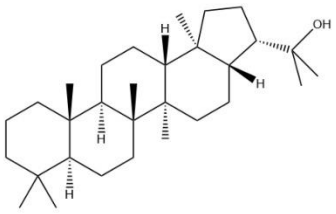

Ⅱ. Diplopterol

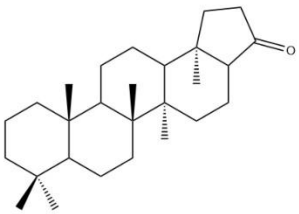

Ⅲ. β-Trisnorhopan-21-one

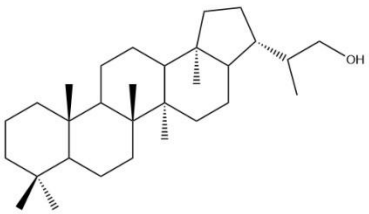

Ⅳ. ββ-Hopanol

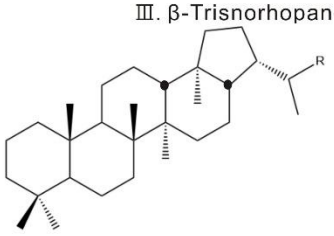

Ⅴ. ββ-Hopanes

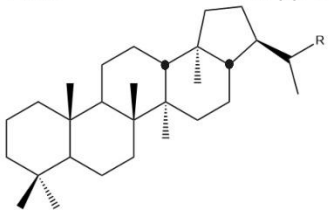

Ⅵ. βα-Moretanes

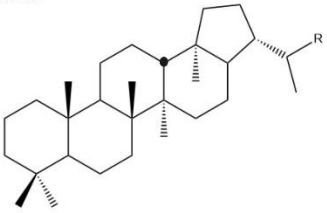

Ⅶ. αβ-Hopanes

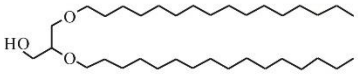

Ⅷ. Non-isoprenoidal dialkyl glycerol diethers

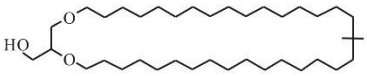

Ⅸ. Macrocyclic glycerol diethers

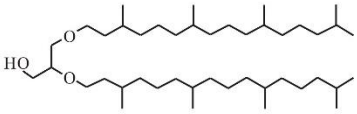

Ⅹ. Archaeol

Appendix 1.

Table 1 The average abundances (and associated indices) for major elements, trace elements and rare earth elements in sediments from the Southwest Indian Ridge

Type	Al_2O_3 (%)	CaO (%)	Fe_2O_3 (%)	K_2O (%)	MgO (%)	MnO (%)	Na_2O (%)	P_2O_5 (%)	TiO_2 (%)	LOI (%)
Background sediments	0.86	44	0.70	0.15	0.50	0.062	1.3	0.053	0.058	5.0
M-T1	2.5	39	2.6	0.17	2.1	0.076	1.6	0.076	0.18	6.9
M-T2	0.25	4.6	21	0.46	1.1	3.8	2.9	0.77	0.017	22
M-T3	1.9	5.6	25	0.18	3.8	1.1	2.0	0.56	0.15	11
Hydrothermal deposits	0.041	0.45	8.9	0.33	0.66	0.95	2.7	0.20	0.003	11

Type	V (ppm)	Cr (ppm)	Co (ppm)	Ni (ppm)	Cu (ppm)	Zn (ppm)	Sr (ppm)	Mo (ppm)	Ba (ppm)	Pb (ppm)
Background sediments	15	11	14	17	30	25	1400	0.62	290	7.8
M-T1	51	68	18	56	280	86	1200	0.70	290	18
M-T2	210	6.0	33	30	2200	740	390	140	360	94
M-T3	340	160	350	90	11000	2300	260	120	160	44
Hydrothermal deposits	66	2.2	3.2	19	45	86	190	150	890	4.8

Type	Li (ppm)	Be (ppm)	Sc (ppm)	Rb (ppm)	Y (ppm)	Zr (ppm)	Nb (ppm)	Cs (ppm)	Hf (ppm)	Th (ppm)
Background sediments	10	0.13	1.8	4.0	8.2	8.9	0.90	0.22	0.31	0.74
M-T1	23	0.16	5.4	4.3	9.0	16	0.79	0.21	0.59	0.62
M-T2	38	0.69	0.63	4.9	9.6	5.6	0.29	0.12	0.13	0.17
M-T3	7.2	0.26	4.9	3.2	11	22	0.80	0.16	0.66	0.58
Hydrothermal deposits	57	0.36	0.76	3.0	1.9	1.0	0.064	0.14	0.023	0.037

Type	U (ppm)	Al/(Al+Fe+Mn)	Fe/Ti	ΣREE (ppm)	ΣREE/Fe (10^{-4})	δCe	δEu
Background sediments	0.31	0.47	14	24	63	0.65	1.2
M-T1	0.32	0.41	18	23	13	0.64	1.3
M-T2	5.3	0.0082	4300	18	1.3	0.56	3.9
M-T3	12	0.054	570	28	1.6	0.63	1.6
Hydrothermal deposits	4.2	0.0041	3900	3.6	0.54	0.66	18

Note: LOI=Loss on ignition, $\delta Ce = Ce_N \Big/ \sqrt{La_N \times Pr_N}$, $\delta Eu = Eu_N \Big/ \sqrt{Sm_N \times Gd_N}$, Ce_N, La_N, Pr_N, Eu_N, Sm_N, Gd_N represent North American shale composite-normalized data.

Table 2 The distributions of *n*-alkanes, *n*-alkanols, sterols and fatty acids in background sediments and M-T1 at the Southwest Indian Ridge

Type	Sample NO.	*n*-alkanes				*n*-alkanols			sterol (ng/g sediment)		LMW/HMW		
		$\sum C_{22}$-C_{34}%	C_{31}%	CPI	ACL	$\sum C_{22}$-C_{34}%	C_{18}%	LMW/HMW	cholesterol	sitosterol	FFAs	GLFAs	PLFAs
background sediments	SW6	76	17	3.4	26	9.5	62	9.5	2.6	0.41	>>1	33	6.0
	SW7	83	25	4.1	27	5.0	68	19	7.1	0.62	44	33	9.0
	SW9	83	24	3.3	27	6.8	78	14	3.8	0.51	57	7.0	2.5
	SW11	75	19	3.0	26	6.0	68	16	7.2	0.75	>>1	12	5.4
	SW12	74	12	1.1	26	21	30	3.7	8.4	1.6	46	4.8	3.4
	SW13	86	16	1.3	27	10	72	8.8	4.1	0.62	20	28	18
	SW17	72	17	3.6	26	7.3	59	13	7.8	0.41	160	26	20
	SW19	83	19	2.5	27	18	18	4.7	8.6	0.60	16	12	20
	SW20	80	21	2.5	27	4.8	65	20	4.2	0.43	200	24	11
	SW21	85	15	2.0	27	15	26	5.5	17	0.86	23	7.3	5.7
	SW22	78	23	4.3	27	5.3	75	18	5.1	–	>>1	8.5	10
	SW27	68	10	1.0	25	5.6	47	17	9.2	1.3	>>1	24	29
	SW28	79	25	4.5	27	5.7	58	17	2.9	0.52	9.0	23	11
	Average	79	19	2.8	27	9.3	56	13	6.8	0.72	>>1	19	12
M-T1	SW2	75	17	2.6	26	23	22	3.3	16	1.2	32	8.9	8.9
	SW3	86	26	3.9	28	7.1	71	13	5.6	0.59	>>1	20	29
	SW4	82	24	4.2	27	6.0	71	16	4.5	0.34	23	25	22
	SW10	84	15	1.2	27	19	66	4.2	9.8	1.00	12	48	19
	Average	82	21	3.0	27	14	58	9	9.0	0.78	>>1	25	20

Note: CPI= carbon preference index, ACL = average chain length, LMW= low molecular weight, HMW= high molecular weight

$$\mathrm{CPI}=\frac{1}{2}\left(\frac{nC_{25}+nC_{27}+nC_{29}+nC_{31}+nC_{33}}{nC_{24}+nC_{26}+nC_{28}+nC_{30}+nC_{32}}+\frac{nC_{25}+nC_{27}+nC_{29}+nC_{31}+nC_{33}}{nC_{26}+nC_{28}+nC_{30}+nC_{32}+nC_{34}}\right)$$

$$\mathrm{ACL}=\frac{\sum 16\times nC_{16}+17\times nC_{17}+18\times nC_{18}+\cdots 34\times nC_{34}}{\sum nC_{16}\text{-}nC_{34}}$$

LMW/HMW= nC_{21}^{-}/nC_{22}^{+}

Table 3 The abundances (ng/g sediment) of specific biomarkers in M-T2 and M-T3 sediments and low-temperature hydrothermal deposits at the Southwest Indian Ridge

Biomarker Type	Sample Type	M-T2			M-T3		low-temperature hydrothermal deposits			
	Sample NO.	SW32	SW38	SW39	SW35	SW40	SW31	SW33	SW36	SW37
n-alkanes	$\sum C_{22}$-C_{34}%	39	–	–	35	30	38	33	50	45
	CPI	1.0	–	–	0.41	0.67	0.80	0.38	0.24	0.70
	ACL	20	18	18	20	20	20	20	21	21
Hopanoids	18α(H)-22, 29, 30-Trisnorhopane (Tm)	–	–	12	–	–	3.8	–	–	–
	22, 29, 30-Trisnorhop-17(21)-ene	3.6	–	–	14	2.3	–	13	–	–
	17α(H)-22, 29, 30-Trisnorhopane (Ts)	–	–	6.1	–	–	2.1	–	–	–
	17β(H)-22, 29, 30-Trisnorhopane	1.3	1.5	–	–	2.0	1.7	6.8	–	–
	17α(H), 21β(H)-30-Norhopane	0.68	8.8	24	4.2	0.83	12	4.0	–	–
	18α(H)-30-Nornehopane	–	–	6.3	–	–	3.4	–	–	–
	17β(H), 21α(H)-30-Normoretane	0.54	–	–	–	–	1.6	3.1	–	–
	Trisnorhopan-21-one	20	18	7.5	62	25	8.4	170	3.7	0.79
	17α(H), 21β(H)-Hopane	–	9.8	24	6.4	3.0	13	–	–	–
	17β(H), 21β(H)-30-Norhopane	2.1	–	–	–	–	–	20	–	–
	22S-17α(H), 21β(H)-Homohopane	–	4.7	10	2.3	–	6.2	–	–	–
	22R-17α(H), 21β(H)-Homohopane	–	4.8	9.3	3.2	3.5	6.8	–	–	–
	C30 diploptene	4.0	–	–	4.9	2.2	2.1	57	–	–
	17β(H), 21α(H)-Hopane	16	9.6	–	8.8	11	15	97	–	–
	22S-17α(H), 21β(H)-Bishomohopane	–	–	8.5	–	–	–	–	–	–
	22R-17α(H), 21β(H)-Bishomohopane	–	–	4.3	–	6.3	–	–	–	–
	17β(H), 21β(H)-Hopane	30	13	–	13	–	15	150	–	–
	22S-17α(H), 21β(H)-Trishomohopane	–	–	4.6	–	–	–	–	–	–
	22R-17α(H), 21β(H)-Trishomohopane	–	–	3.2	–	–	–	–	–	–
	22S-17β(H), 21α(H)-Homomoretane	28	9.4	–	5.9	24	9.2	110	–	–
	22R-17β(H), 21α(H)-Homomoretane	36	7.7	–	7.5	6.0	13	200	–	–
	ββ-hopan-30-ol	12	73	18	41	58	7.4	–	12	2.5
	Diplopterol	26	–	2.8	13	4.7	9.3	140	–	–
	22S-17β(H), 21α(H)-Bishomomoretane	–	–	–	–	–	23	140	–	–
	22S-17β(H), 21α(H)-Trishomomoretane	9.4	–	–	–	–	14	54	–	–
	22S-17α(H),	5.6	–	–	–	–	4.5	23	–	–

	21β(H)-Trishomohopane									
	17β(H), 21α(H)-Tetrashomomoretane	9.3	–	–	–	–	2.9	–	–	–
	17β(H),21β(H)-Bishomohopan-32-ol	12	23	5.8	28	15	12	48	–	2.0
	C31 hopane 22S/(22S+22R)	–	0.50	0.52	0.41	–	0.48	–	–	–
DGD	C13/C14	–	–	–	–	13	–	–	–	–
	C15/C14a	–	–	–	–	12	–	–	–	–
	C15/C14b	–	–	–	–	18	–	–	–	–
	C15/C15a	–	–	–	–	22	–	–	–	–
	C15/C15b	–	6.7	–	–	12	–	–	–	1.7
	C15/C15c	–	8.9	–	–	19	–	–	–	–
	C17/C16	–	–	–	–	–	–	30	–	–
	C17/C17a	–	4.8	–	–	7.2	–	–	–	–
	C17/C17b	25	21	–	12	6.9	5.2	33	–	–
	C17/C17c	–	–	–	–	–	–	34	–	–
	C16/C18	–	–	–	–	7.9	–	–	–	–
	C19/C17	–	–	–	–	11	–	5.8	–	–
	C17:1/C17:1	–	–	–	–	2.8	–	14	–	–
McGD	C31	–	–	–	6.4	–	–	–	–	–
	C34	11	–	–	–	–	2.6	9.6	–	–
	C35	–	–	–	2.7	–	–	–	–	–
archaeol		2.4	21	2.5	9.3	120	2.7	19	1.6	16

Note that a, b, c represent different unknown alkyl chains and these contents of different biomarkers in hydrothermal deposits SW41, SW45 and SW46 are not calculated due to the low abundance.